Observation of Boron Carbonyl Complexes $B_{11}(CO)_n^+$ (n = 1-6) and $B_{15}(CO)_n^+$ (n =1-5) with Conflicting Aromaticity

Rui-Nan Yuan,[a] Qiang Chen,*[a] Hong Niu,[a] Cai-Yue Gao,[a] Xiao-Ni Zhao,[a] Yan-Bo Wu,[a] Sheng-Gui He,*[b] Si-Dian Li*[a]

[a] Institute of Molecular Science, Shanxi University, Taiyuan 030006, P. R. China
[b] State Key Laboratory for Structural Chemistry of Unstable and Stable Species, Institute of Chemistry, Chinese Academy of Sciences, Beijing 100190, P. R. China
E-mail: chenqiang@sxu.edu.cn; shengguihe@iccas.ac.cn; lisidian@sxu.edu.cn.

Table of Contents

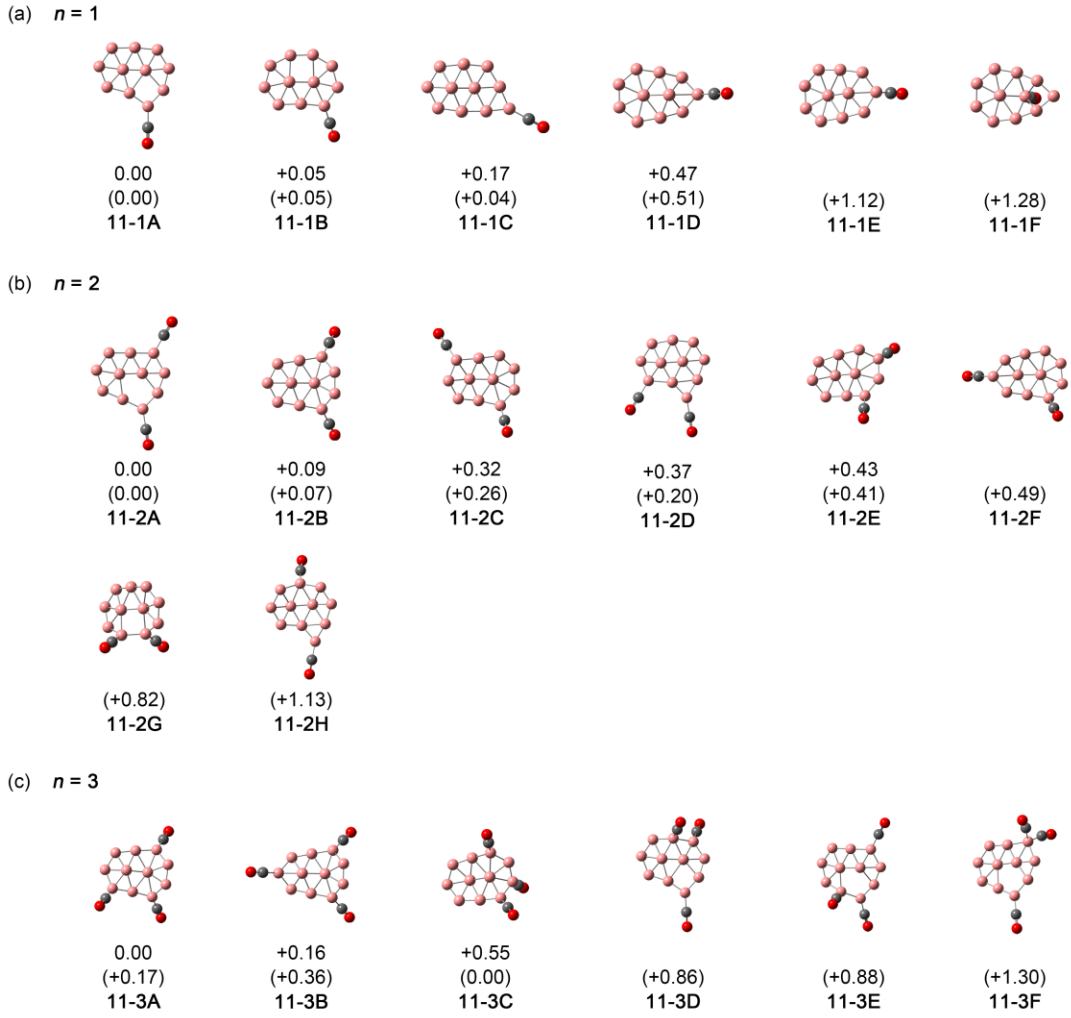

Fig. S1. Optimized low-lying isomers of $B_{11}(CO)_n^+$ (n = 1-3) at PBE0/6-311-G(d,p) level, with the relative energies (ΔE) indicated in eV at CCSD(T)/6-311+G(d,p)//PBE0/6-311+G(d,p) and PBE0/6-311+G(d,p) (in parentheses) levels, respectively.

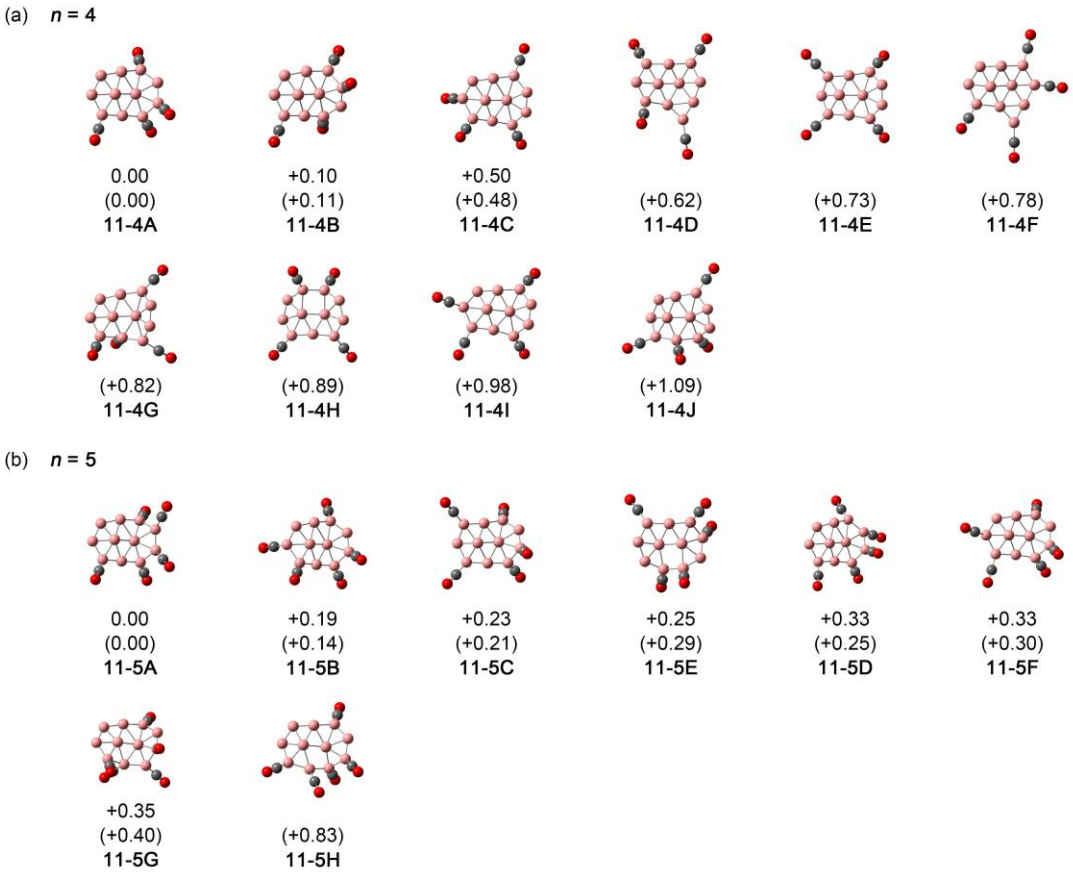

Fig. S2. Optimized low-lying isomers of $B_{11}(CO)_n^+$ (n = 4-5) at PBE0/6-311-G(d,p) level, with the relative energies (ΔE) indicated in eV at CCSD(T)/6-311+G(d,p)//PBE0/6-311+G(d,p) and PBE0/6-311+G(d,p) (in parentheses), respectively.

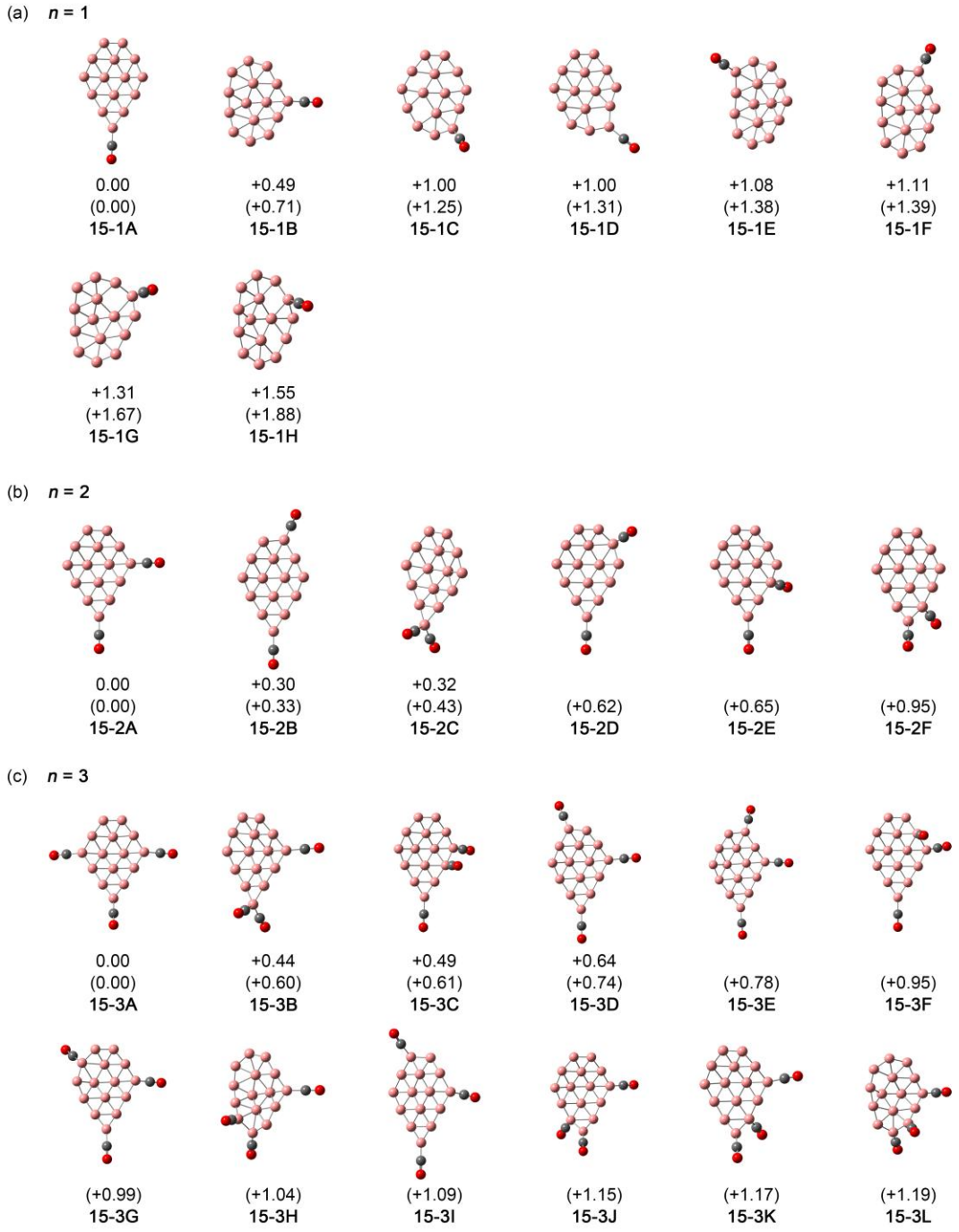

Fig. S3. Optimized low-lying isomers of $B_{15}(CO)_n^+$ (n = 1-3) at PBE0/6-311-G(d,p) level, with the relative energies (ΔE) indicated in eV at CCSD(T)/6-311+G(d,p)//PBE0/6-311+G(d,p) and PBE0/6-311+G(d,p) (in parentheses), respectively.

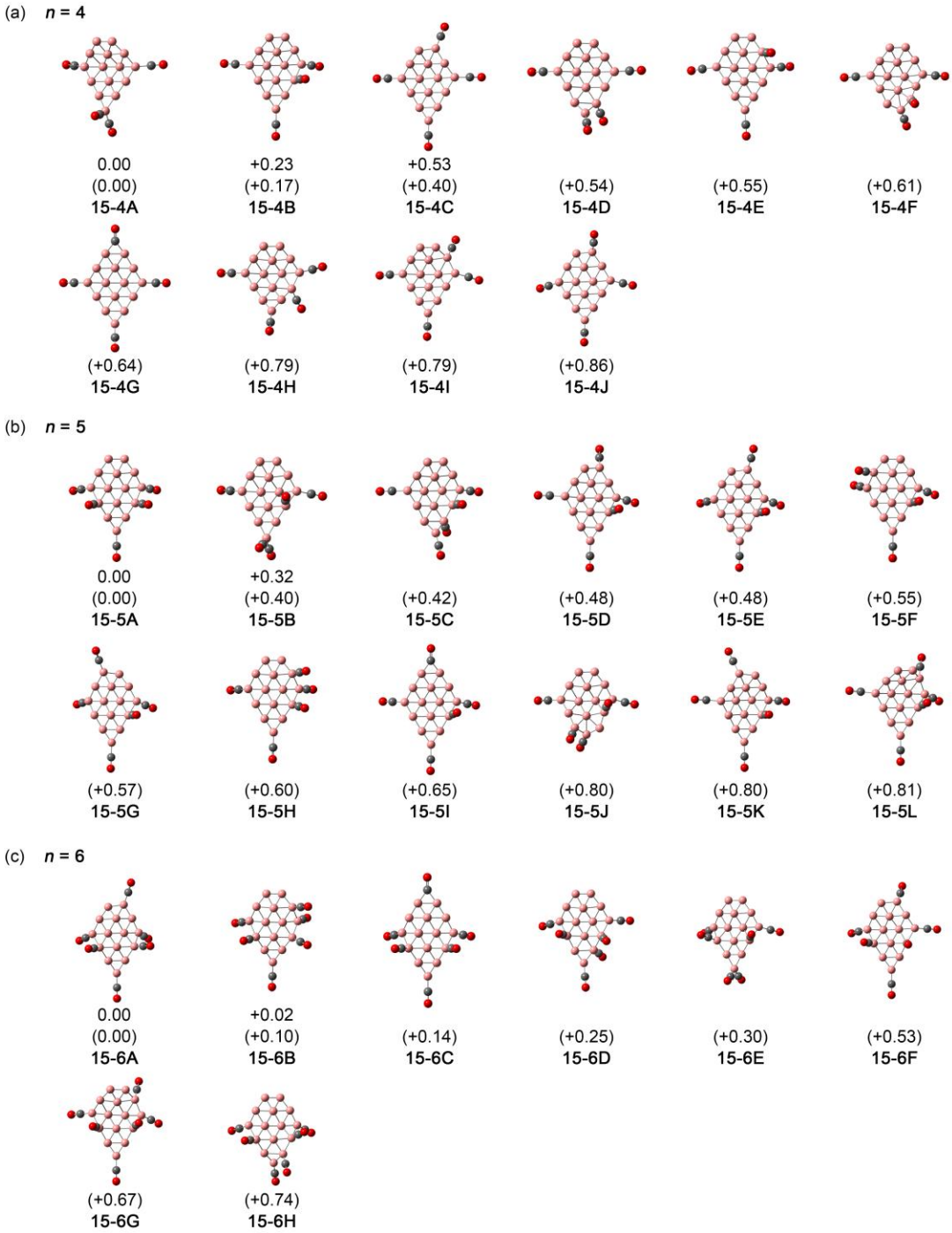

Fig. S4. Optimized low-lying isomers of $B_{15}(CO)_n^+$ (n = 4-6) at PBE0/6-311-G(d,p) level, with the relative energies (ΔE) indicated in eV at CCSD(T)/6-311+G(d,p)//PBE0/6-311+G(d,p) and PBE0/6-311+G(d,p) (in parentheses) levels, respectively.

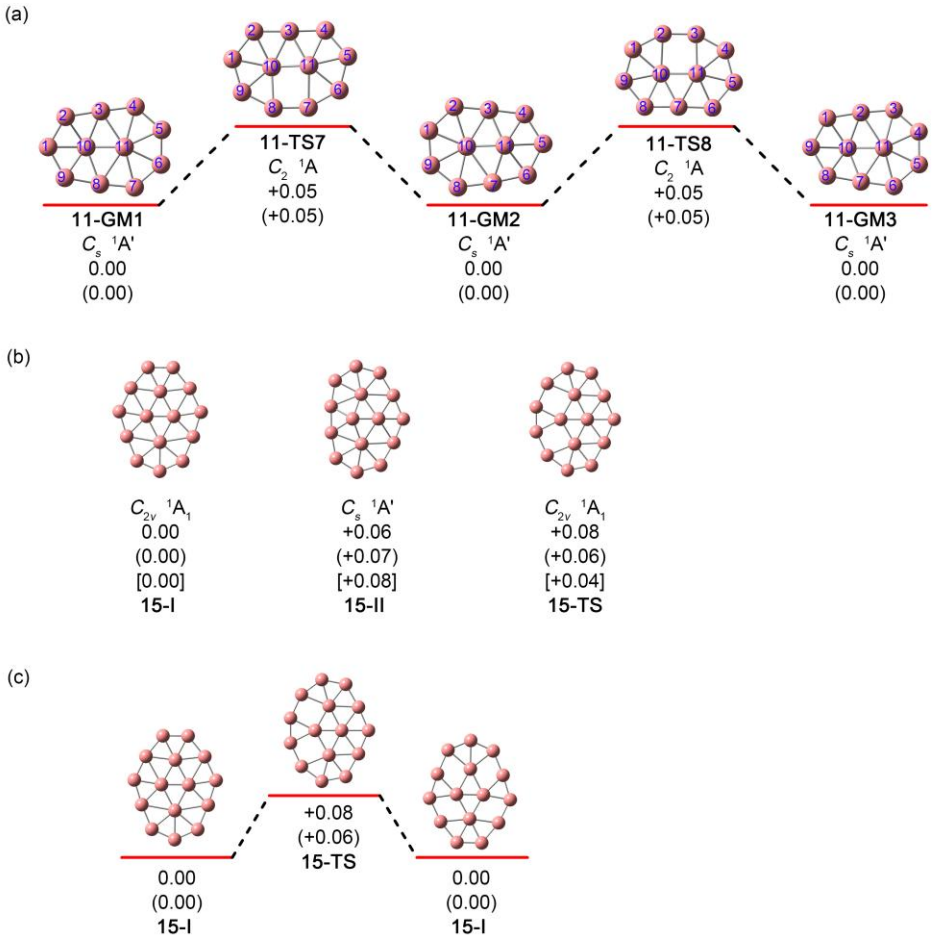

Fig. S5. (a) Optimized fluxional mechanism of B_{11}^+, with the relative energies indicated in eV at CCSD(T)/6-311+G(d,p)//PBE0/6-311+G(d,p) and PBE0/6-311+G(d,p) (in parentheses) levels, respectively. (b) Optimized structures of B_{15}^+ with the relative energies indicated in eV at CCSD(T)/6-311+G(d,p)//PBE0/6-311+G(d,p), PBE0/6-311+G(d,p) (in parentheses), TPSSh/def2-TZVPP (square bracket), respectively. (c) Optimized fluxional mechanism of C_{2v} B_{15}^+ (**15-I**), with the relative energies indicated eV at CCSD(T)/6-311+G(d,p)//PBE0/6-311+G(d,p) and PBE0/6-311+G(d,p) (in parentheses), respectively.

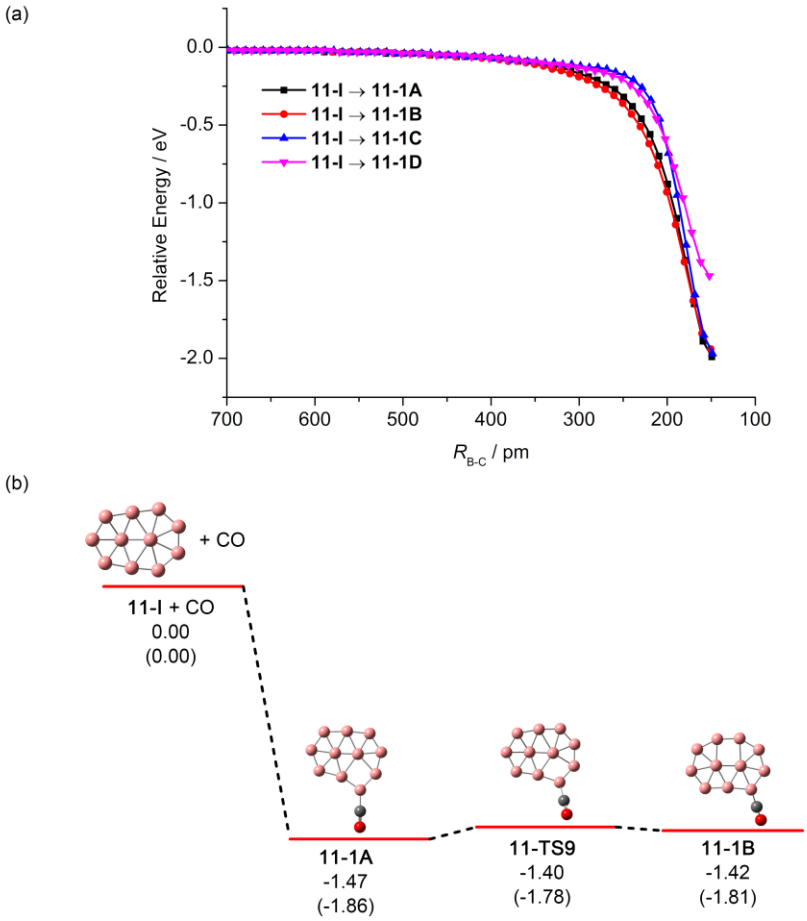

Fig. S6. (a) Calculated relaxed potential energy curves for the approach of CO toward B_{11}^+ at PBE0/6-311+G(d,p). (b) Calculated potential energy profile to form **11-1A** and **11-1B**, with the relative energies indicated in eV for the intermediate states (Is) and transition states (TSs) at CCSD(T)/6-311+G(d,p)//PBE0/6-311+G(d,p) and PBE0/6-311+G(d,p) (in parentheses), respectively.

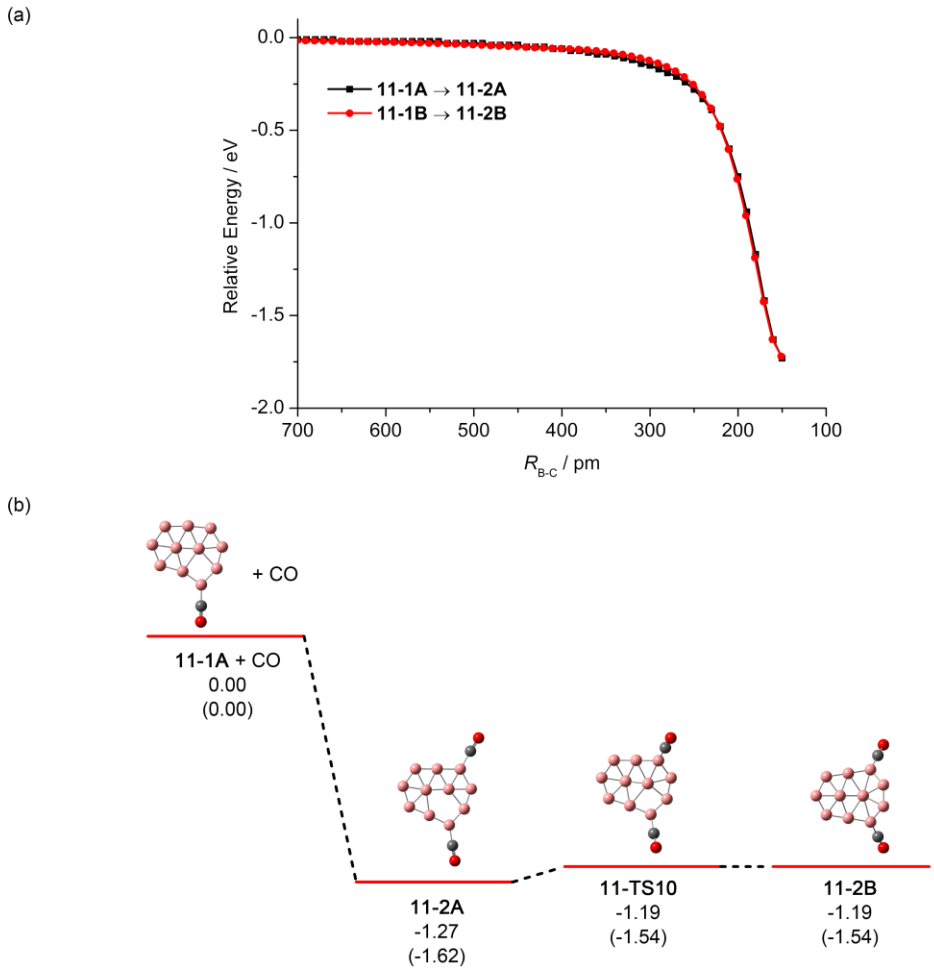

Fig. S7. (a) Calculated relaxed potential energy curves for the approach of CO toward **11-1A** and **11-1B** at PBE0/6-311+G(d,p). (b) Calculated potential energy profile to form **11-2A** and **11-2B,** with the relative energies indicated in eV for the intermediate states (Is) and transition states (TSs) at CCSD(T)/6-311+G(d,p)//PBE0/6-311+G(d,p) and PBE0/6-311+G(d,p) (in parentheses), respectively.

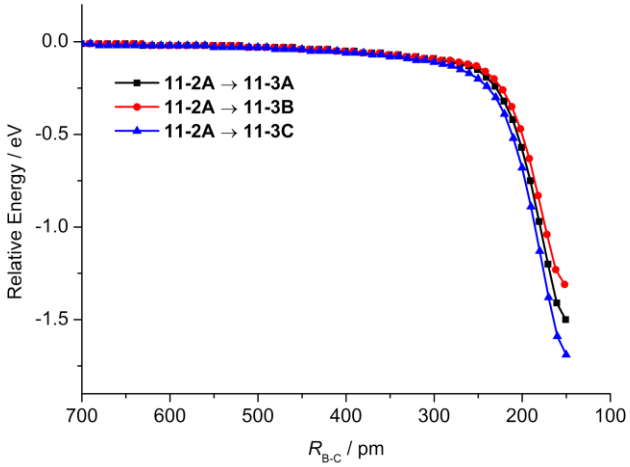

Fig. S8. Calculated relaxed potential energy curves for the approach of CO toward **11-2B** to form **11-3A**, **11-3B** and **11-3C** at PBE0/6-311+G(d,p).

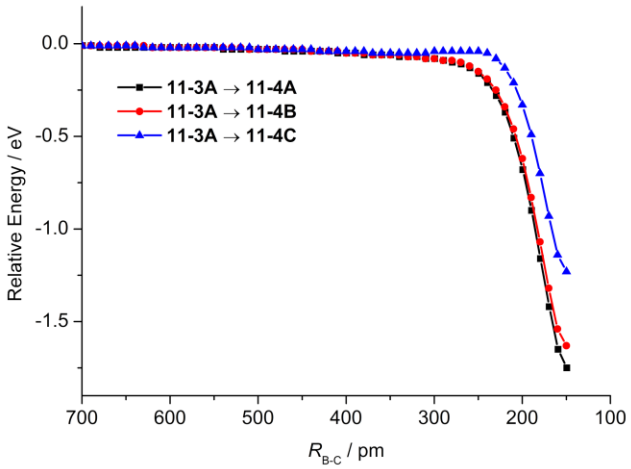

Fig. S9. Calculated relaxed potential energy curves for the approach of CO toward **11-3A** to form **11-4A**, **11-4B** and **11-4C** at PBE0/6-311+G(d,p).

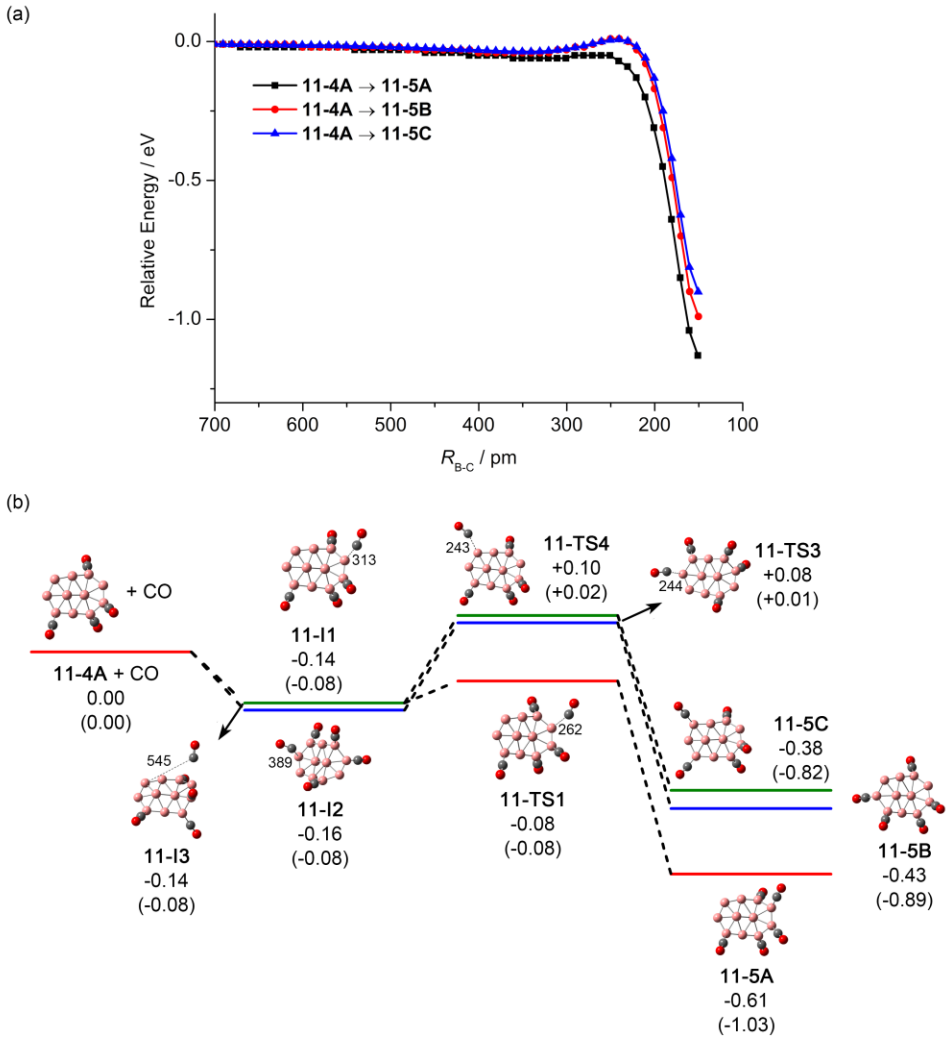

Fig. S10. (a) Calculated relaxed potential energy curves for the approach of CO toward **11-4A** at PBE0/6-311+G(d,p). (b) Calculated potential energy profile to form **11-5A**, **11-5B** and **11-5C**, with the relative energies indicated in eV for the intermediate states (Is) and transition states (TSs) at CCSD(T)/6-311+G(d,p)//PBE0/6-311+G(d,p) and PBE0/6-311+G(d,p) (in parentheses), respectively. The relative energies are in units of eV and bond lengths are given in pm.

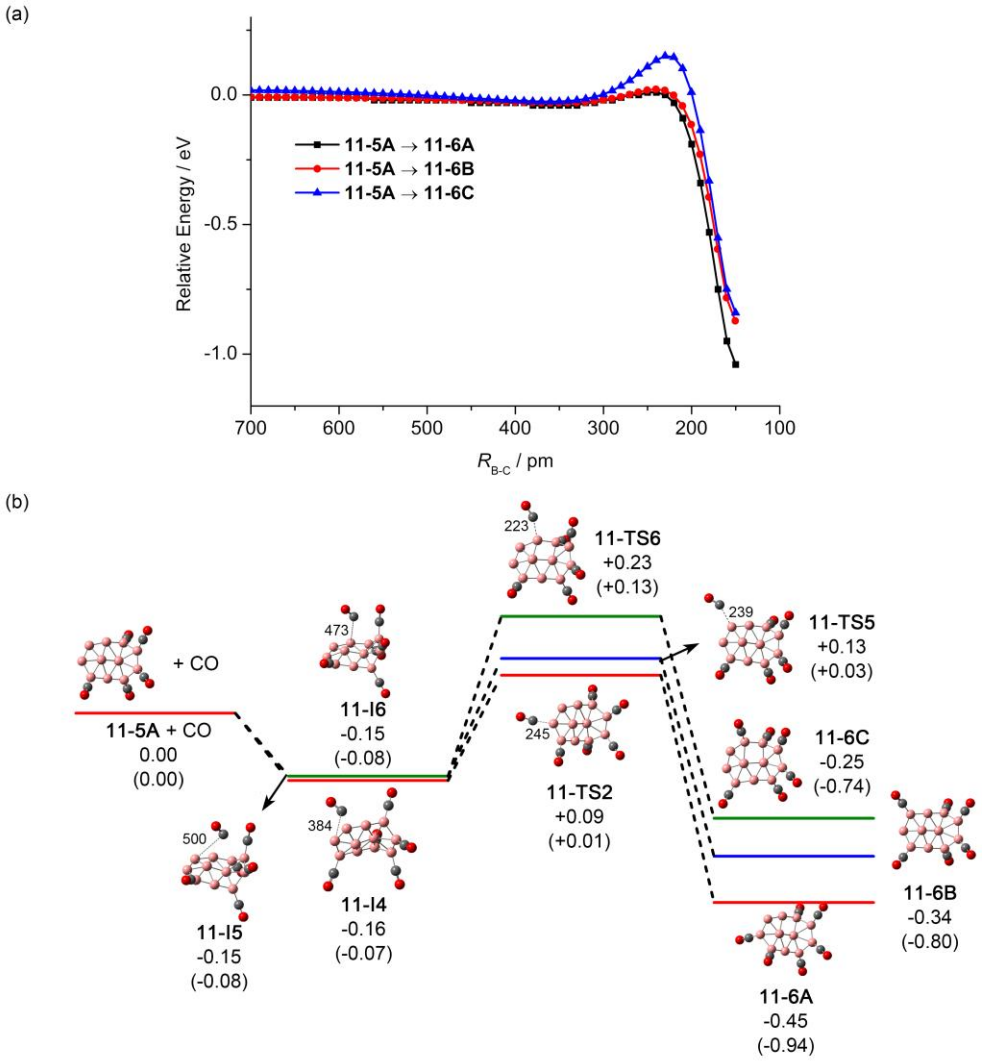

Fig. S11. (a) Calculated relaxed potential energy curves for the approach of CO toward **11-5A** at PBE0/6-311+G(d,p). (b) Calculated potential energy profile to form **11-6A**, **11-6B** and **11-6C**, with the relative energies indicated in eV for the intermediate states (Is) and transition states (TSs) at CCSD(T)/6-311+G(d,p)//PBE0/6-311+G(d,p) and PBE0/6-311+G(d,p) (in parentheses), respectively. The relative energies are in units of eV and bond lengths are given in pm.

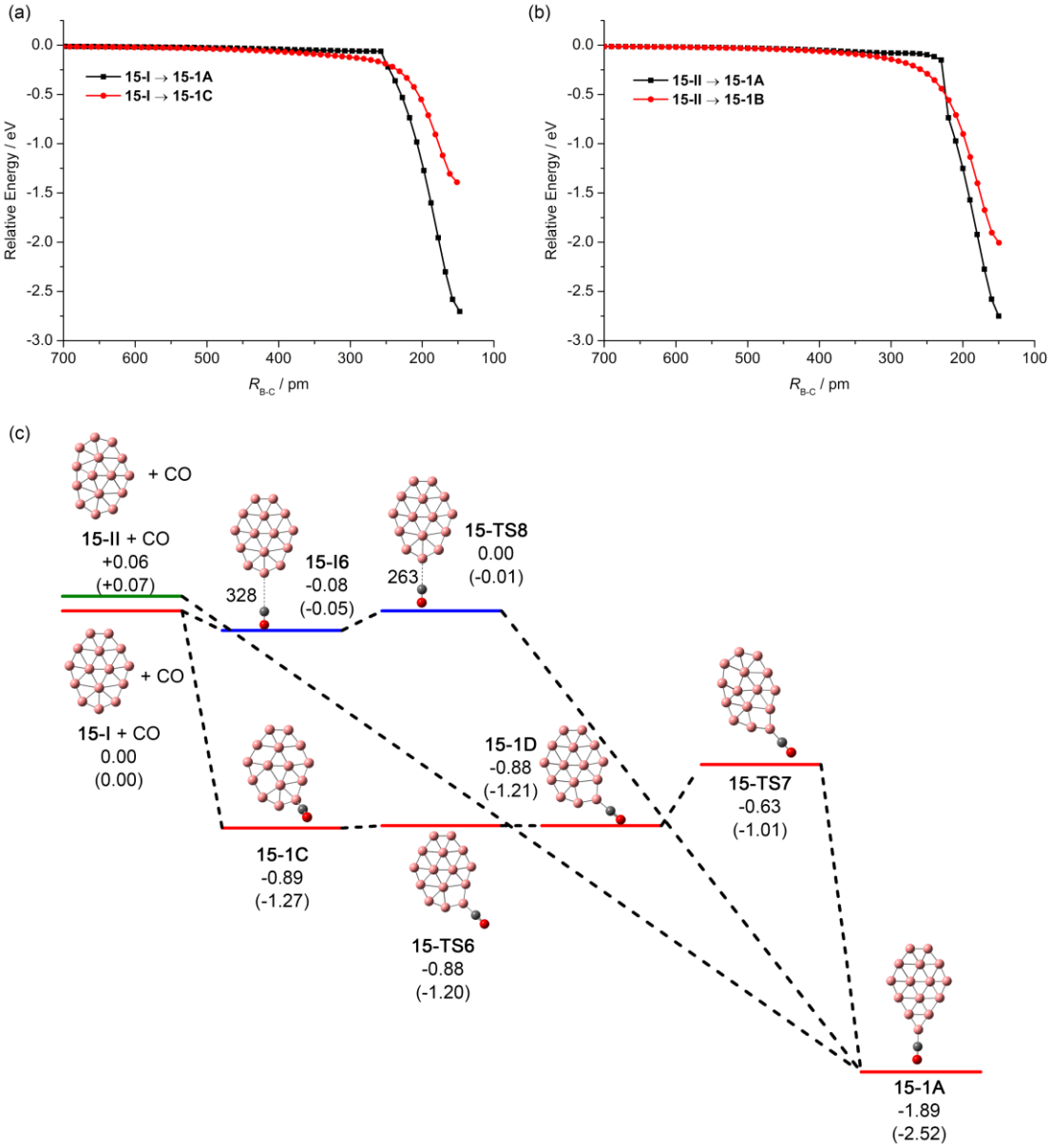

Fig. S12. Calculated relaxed potential energy curves for the approach of CO toward **15-I** (a) to form **15-1A** and **15-1C** and **15-II** (b) to form **15-1A** and **15-1B** at PBE0/6-311+G(d,p). (c) Calculated potential energy profile to form **15-1A**, with the relative energies indicated in eV for the intermediate states (Is) and transition states (TSs) at CCSD(T)/6-311+G(d,p)//PBE0/6-311+G(d,p) and PBE0/6-311+G(d,p) (in parentheses), respectively.

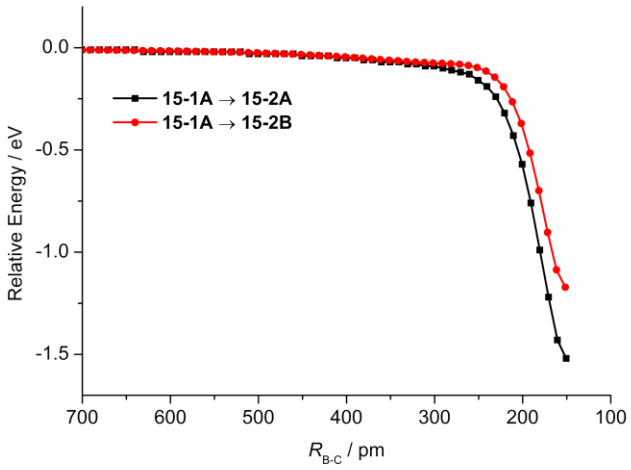

Fig. S13. Calculated relaxed potential energy curves for the approach of CO toward **15-1A** to form **15-2A** and **15-2B** at PBE0/6-311+G(d,p).

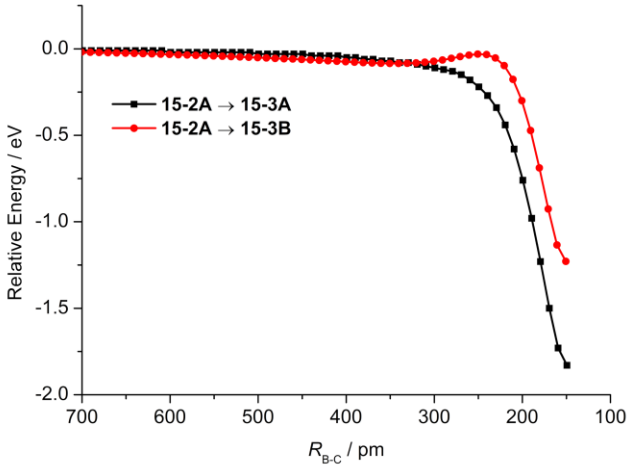

Fig. S14. Calculated relaxed potential energy curves for the approach of CO toward **15-2A** to form **15-3A** and **15-3B** at PBE0/6-311+G(d,p).

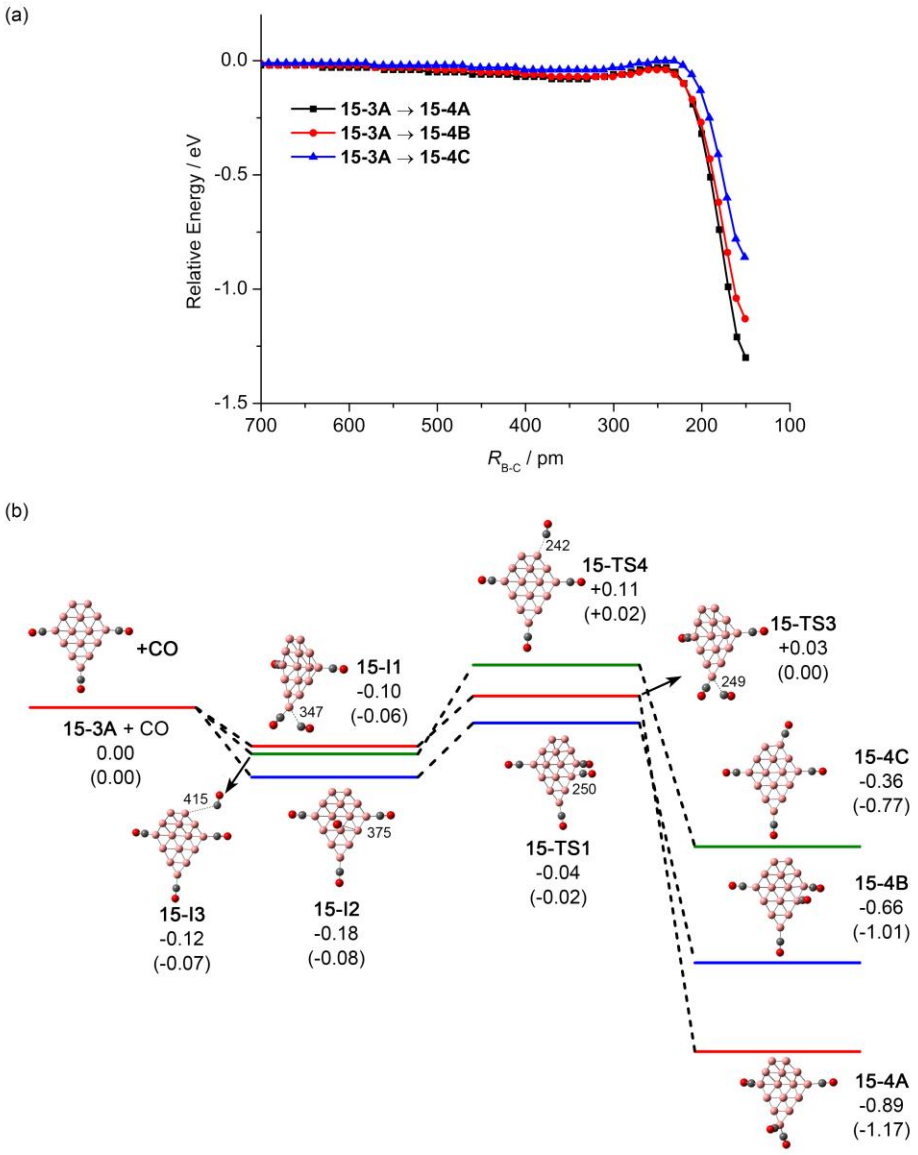

Fig. S15. (a) Calculated relaxed potential energy curves for the approach of CO toward **15-3A** at PBE0/6-311+G(d,p). (b) Calculated potential energy profile to form **15-4A**, **15-4B** and **15-4C**, with the relative energies indicated in eV for the intermediate states (Is) and transition states (TSs) at CCSD(T)/6-311+G(d,p)//PBE0/6-311+G(d,p) and PBE0/6-311+G(d,p) (in parentheses), respectively. The relative energies are in units of eV and bond lengths are given in pm.

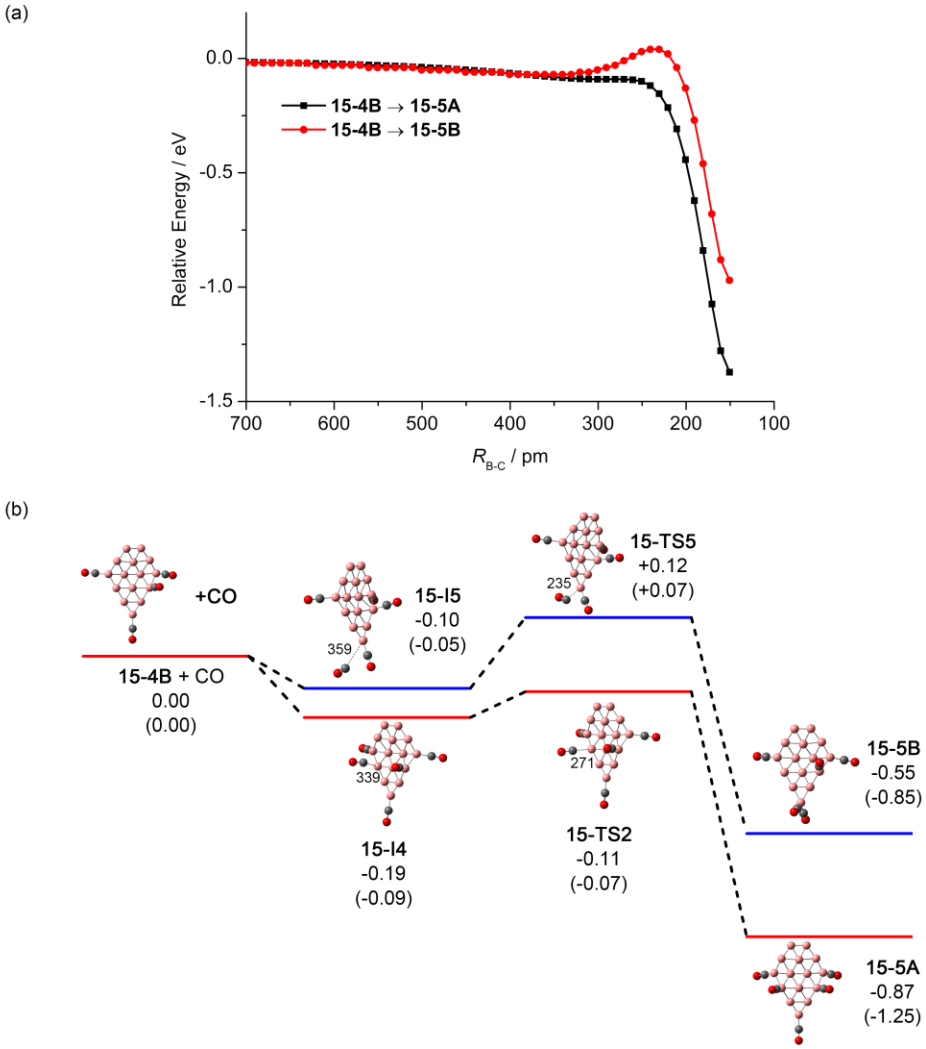

Fig. S16. (a) Calculated relaxed potential energy curves for the approach of CO toward **15-4B** at PBE0/6-311+G(d,p). (b) Calculated potential energy profile to form **15-5A**, and **15-5B**, with the relative energies indicated in eV for the intermediate states (Is) and transition states (TSs) at CCSD(T)/6-311+G(d,p)//PBE0/6-311+G(d,p) and PBE0/6-311+G(d,p) (in parentheses), respectively. The relative energies are in units of eV and bond lengths are given in pm.

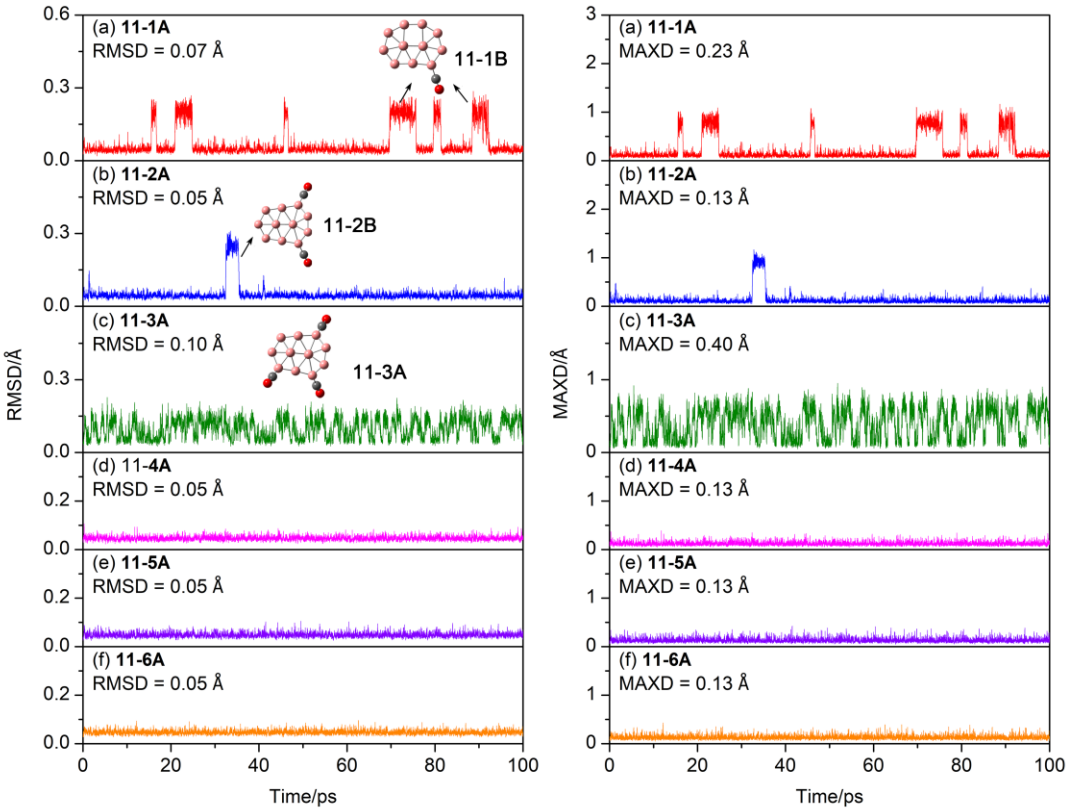

Fig. S17. Born-Oppenheimer molecular dynamics (BOMD) simulations of (a) C_s **B_{11}-1A**, (b) C_s **B_{11}-2A**, (c) C_1 **B_{11}-3A**, (d) C_1 **B_{11}-4A**, (e) C_1 **B_{11}-5A**, and (f) C_1 **B_{11}-6A** at 300K for 100 ps, with the calculated average root-mean-square-deviations (RMSD) values and maximum bond length deviations (MAXD) values indicated.

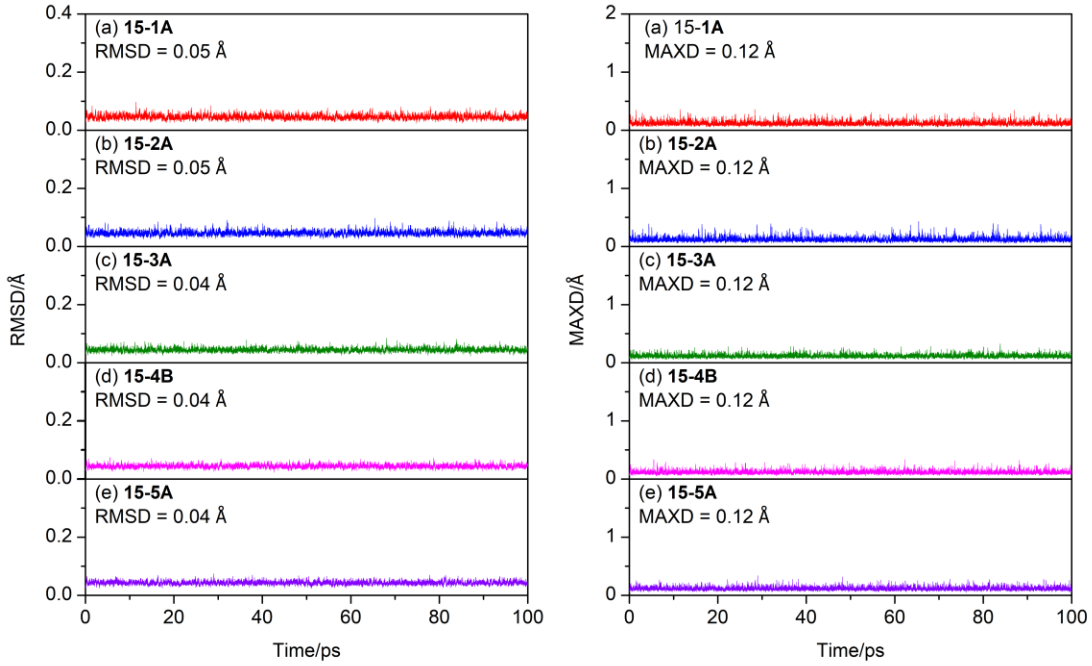

Fig. S18. Born-Oppenheimer molecular dynamics (BOMD) simulations of (a) C_s **B_{15}-1A**, (b) C_1 **B_{15}-2A**, (c) C_s **B_{15}-3A**, (d) C_1 **B_{15}-4B** and (e) C_s **B_{15}-5A** at 300K for 100 ps. The calculated average root-mean-square-deviations (RMSD) values and maximum bond length deviations (MAXD) values are indicated.

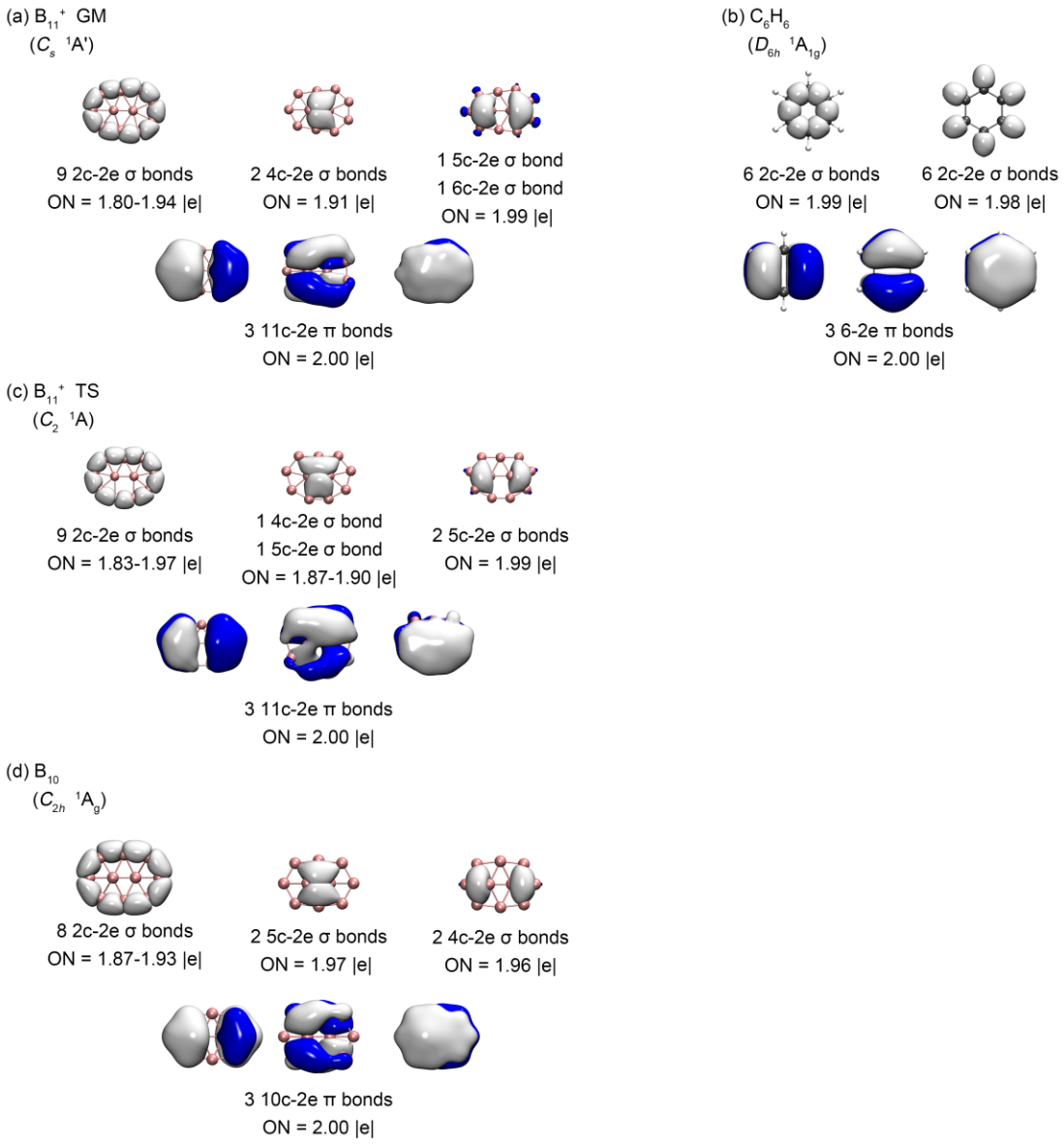

Fig. S19. AdNDP bonding patterns of (a) C_s B_{11}^+ GM, (b) D_{6h} C_6H_6, (c) C_2 B_{11}^+ TS, and (d) C_{2h} B_{10}, with the occupation numbers (ONs) indicated.

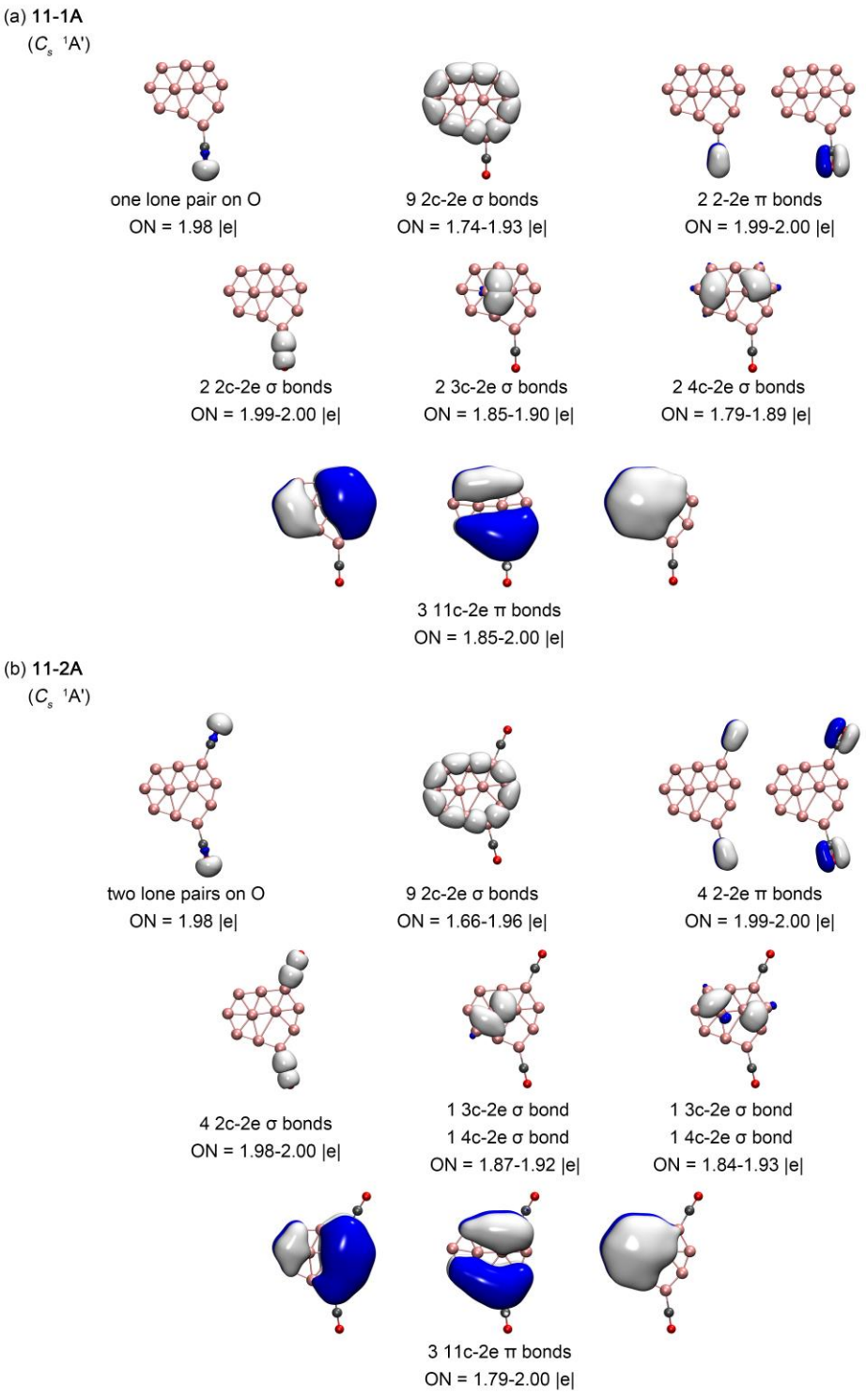

Fig. S20. AdNDP bonding patterns of (a) C_s **B_{11}-1A** and (b) C_s **B_{11}-2A**, with the occupation numbers (ONs) indicated.

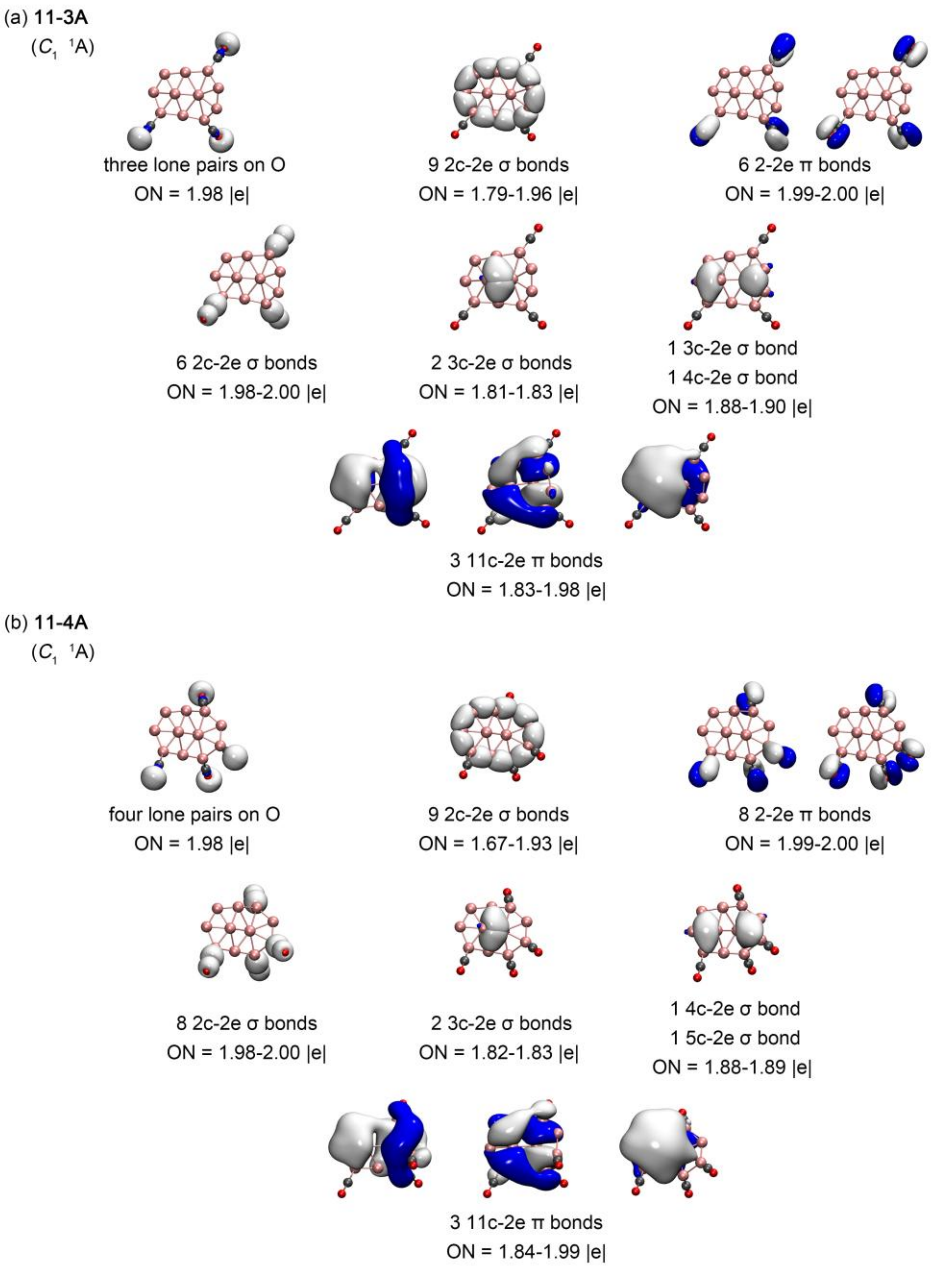

Fig. S21. AdNDP bonding patterns of (a) C_1 **B_{11}-3A** and (b) C_1 **B_{11}-4A**, with the occupation numbers (ONs) indicated.

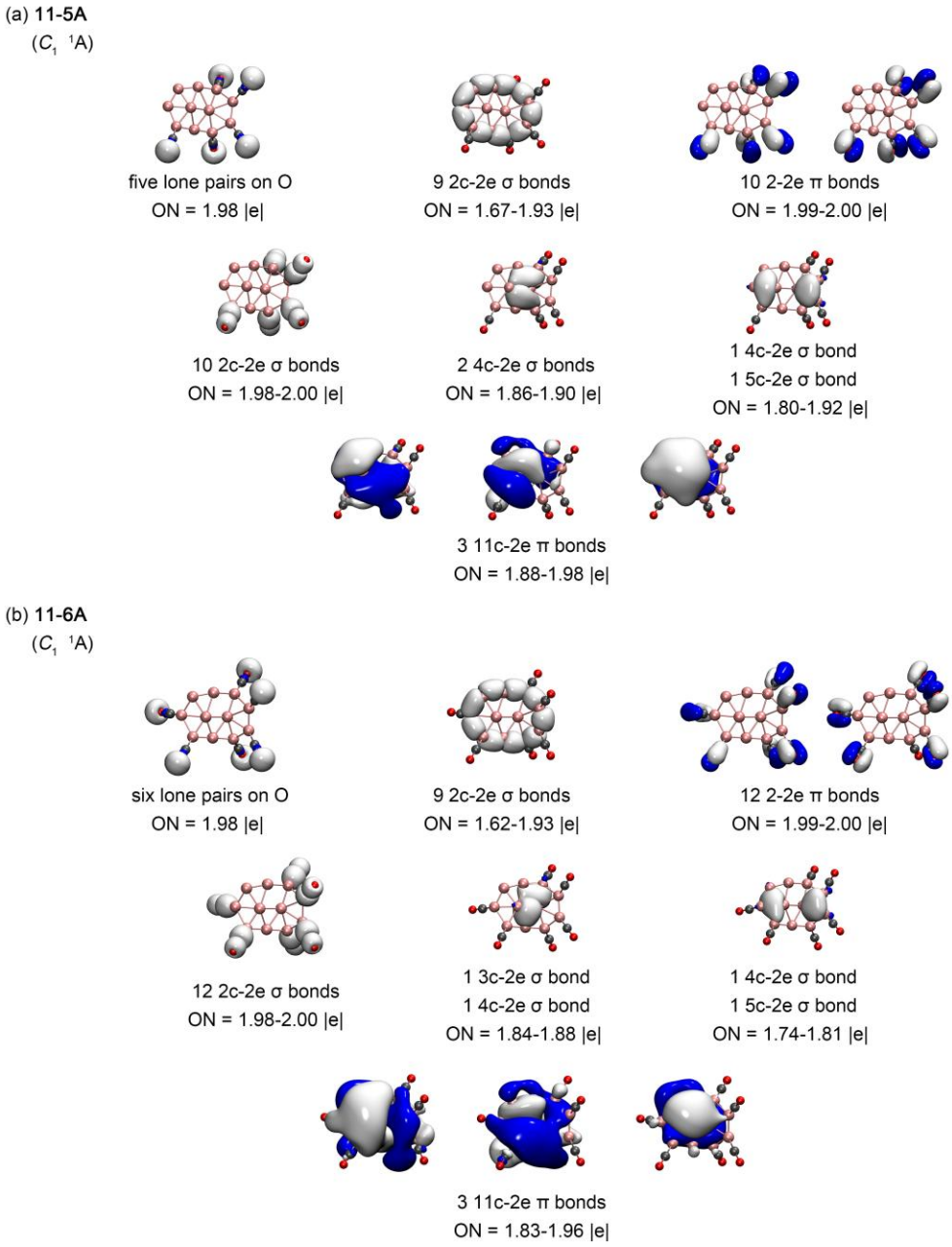

Fig. S22. AdNDP bonding patterns of (a) C_1 **B_{11}-5A** and (b) C_1 **B_{11}-6A**, with the occupation numbers (ONs) indicated.

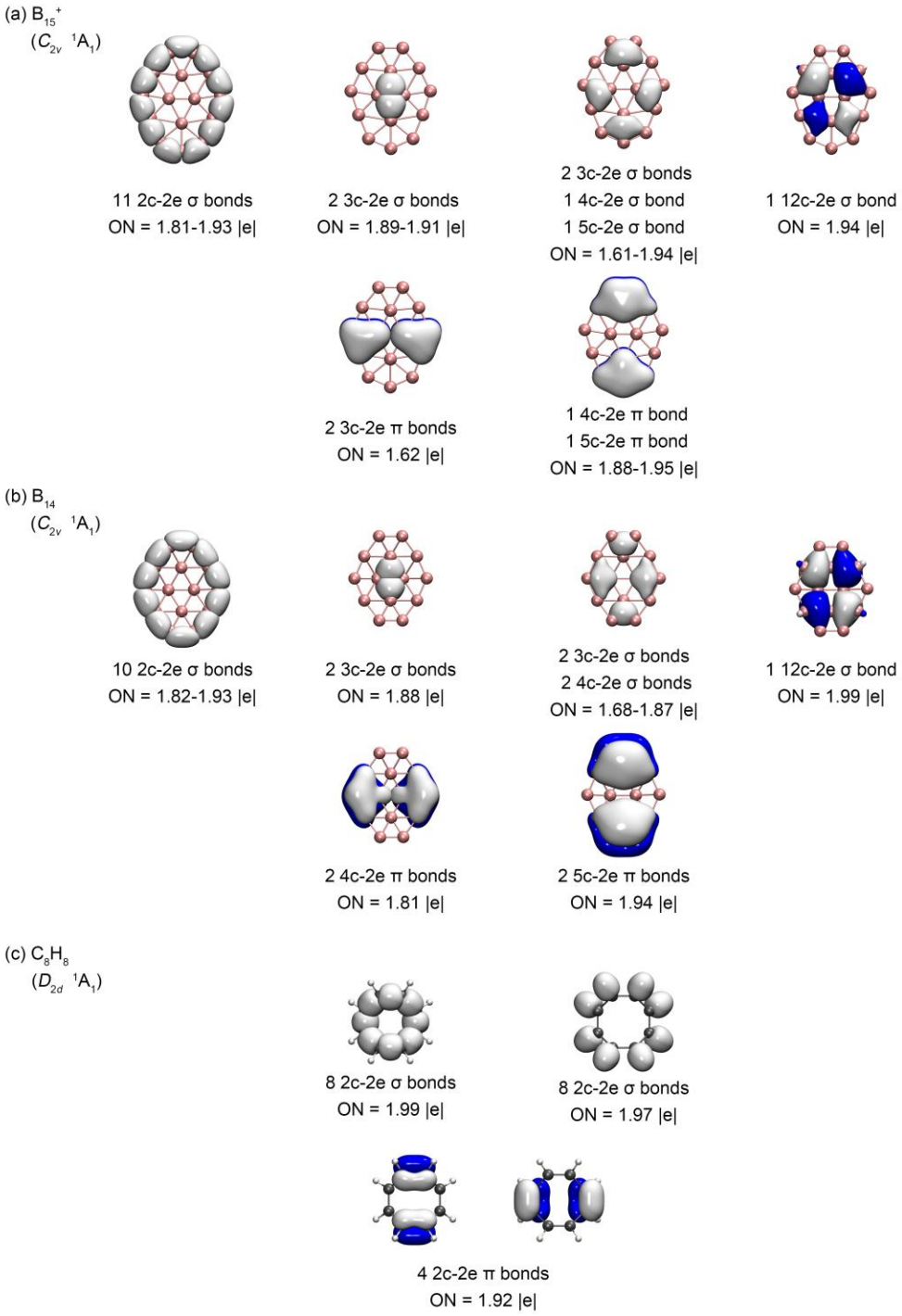

Fig. S23. AdNDP bonding patterns of (a) C_{2v} B_{15}^+, (b) C_{2v} B_{14}, and (c) D_{2d} C_8H_8, with the occupation numbers (ONs) indicated.

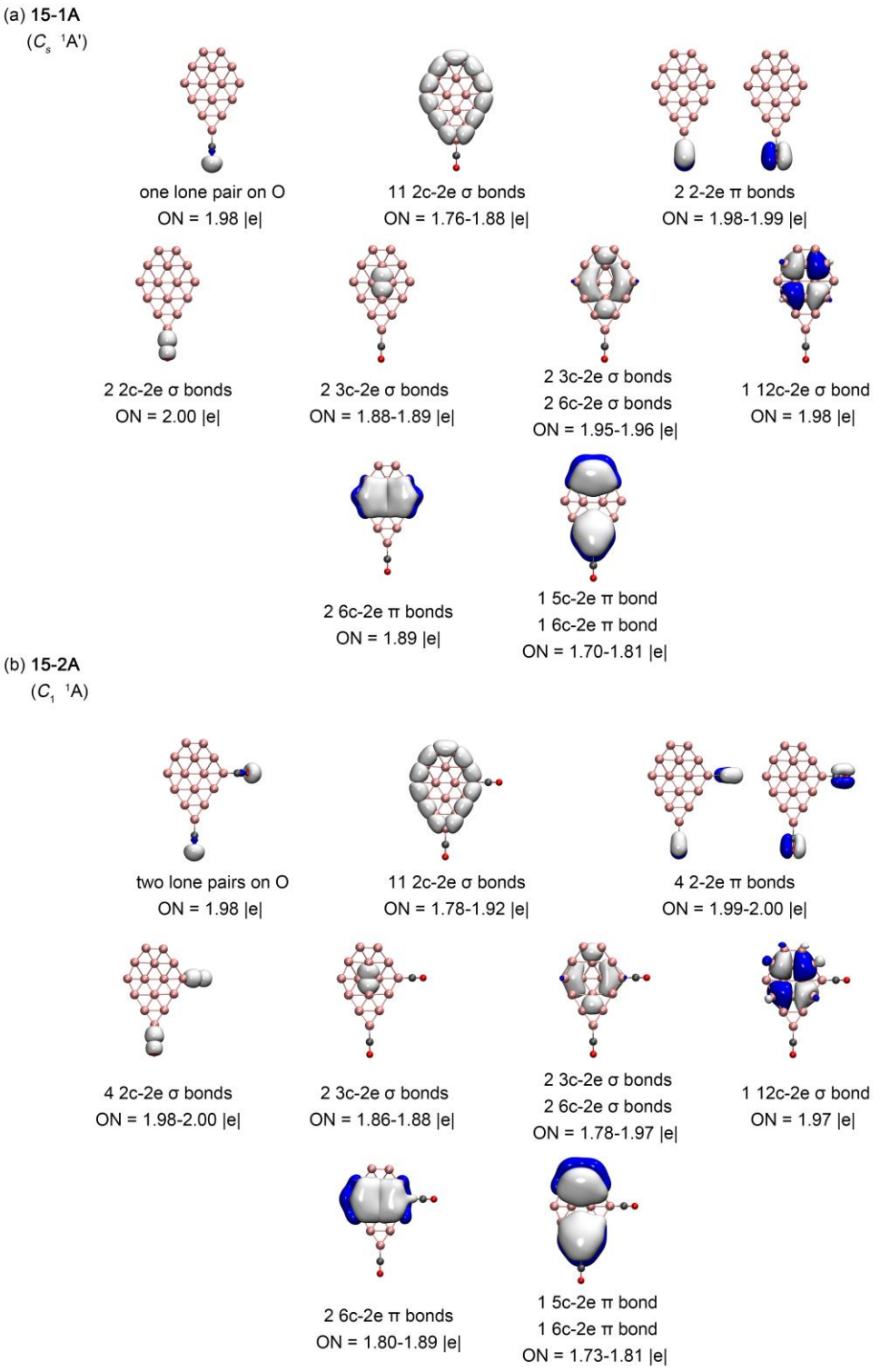

Fig. S24. AdNDP bonding patterns of (a) C_s **B_{15}-1A** and (b) C_1 **B_{15}-2A**, with the occupation numbers (ONs) indicated.

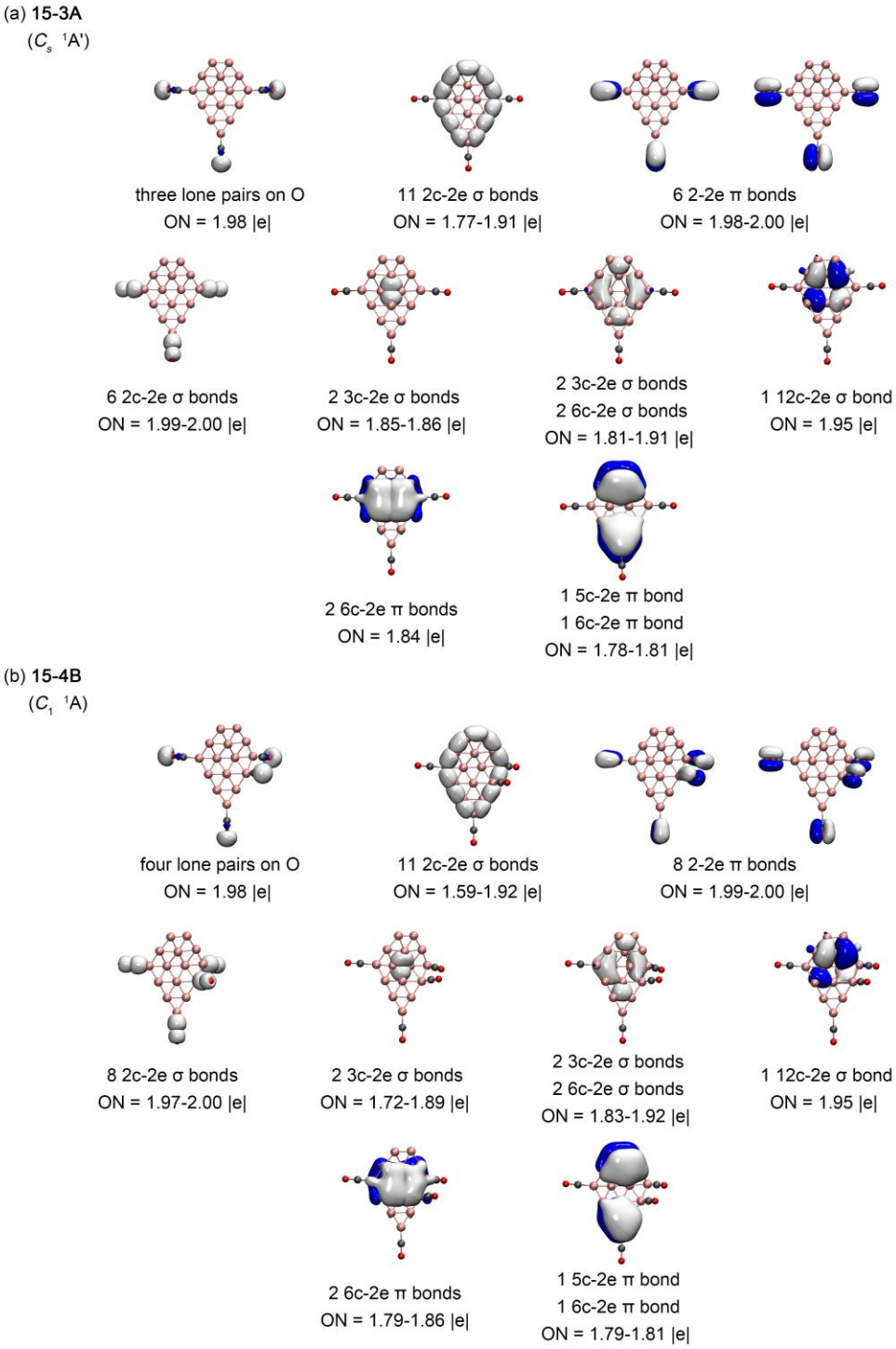

Fig. S25. AdNDP bonding patterns of (a) C_s **B_{15}-3A** and (b) C_1 **B_{15}-4B**, with the occupation numbers (ONs) indicated.

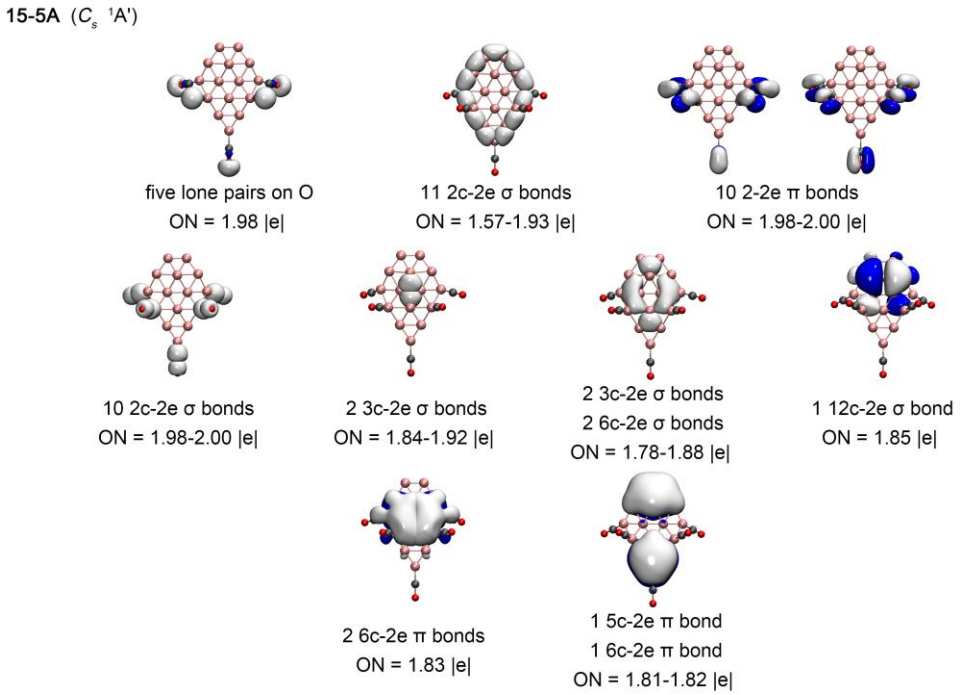

Fig. S26. AdNDP bonding patterns of C_s **B_{15}-5A**, with the occupation numbers (ONs) indicated.

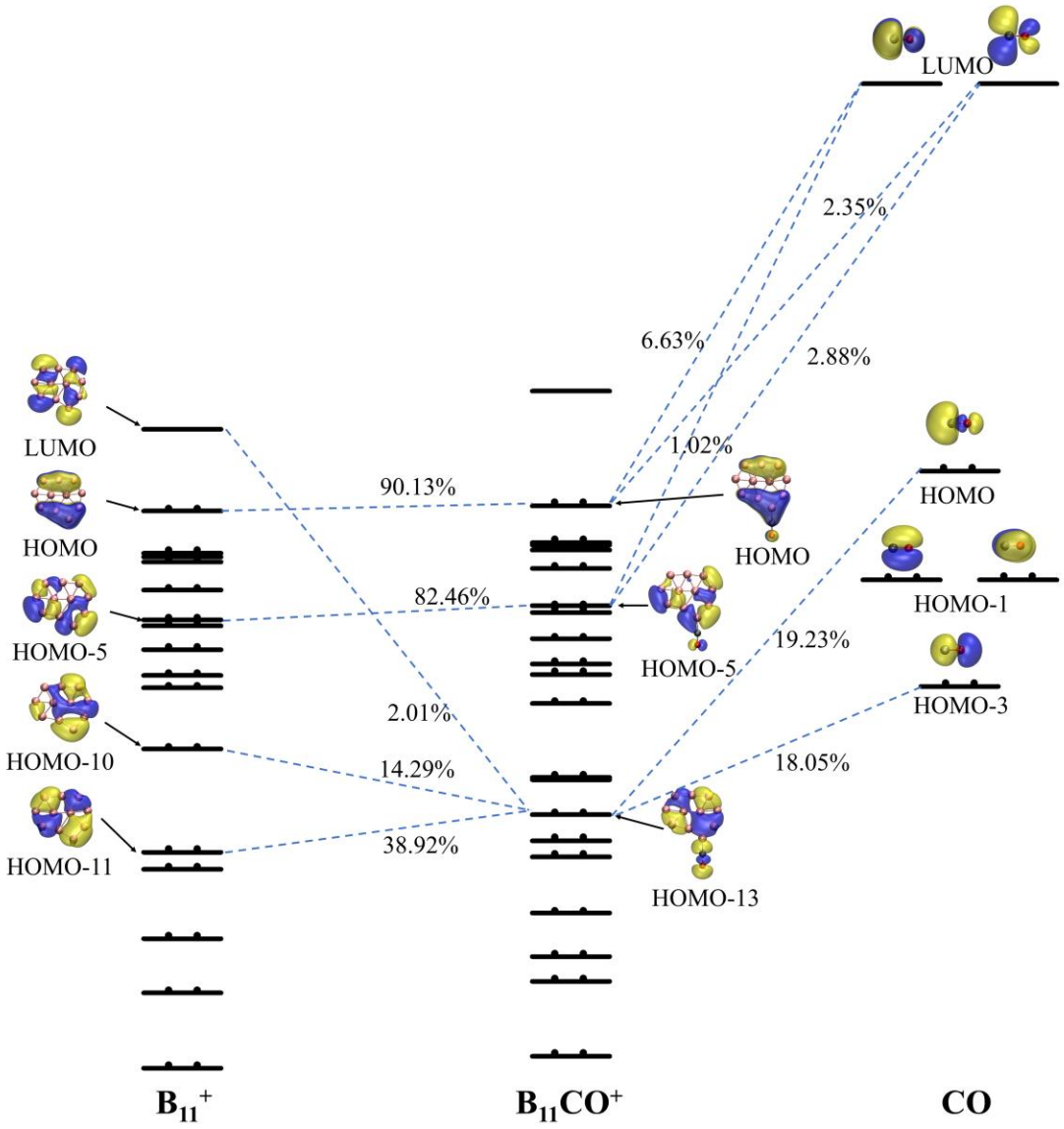

Fig. S27. Bonding scheme of $B_{11}(CO)^+$ (**11-1A**) based on EDA-NOCV analyses, with C_s B_{11}^+ and CO designated as interacting fragments. Only the most important occupied valence orbitals HOMO-13 representing the effective σ-donation coordination bond and HOMO and HOMO-5 responsible for weak π-back-donations between B_{11}^+ and its ligand CO are shown, with the percentage contributions from the corresponding molecular orbitals of the fragments B_{11}^+ and CO indicated.

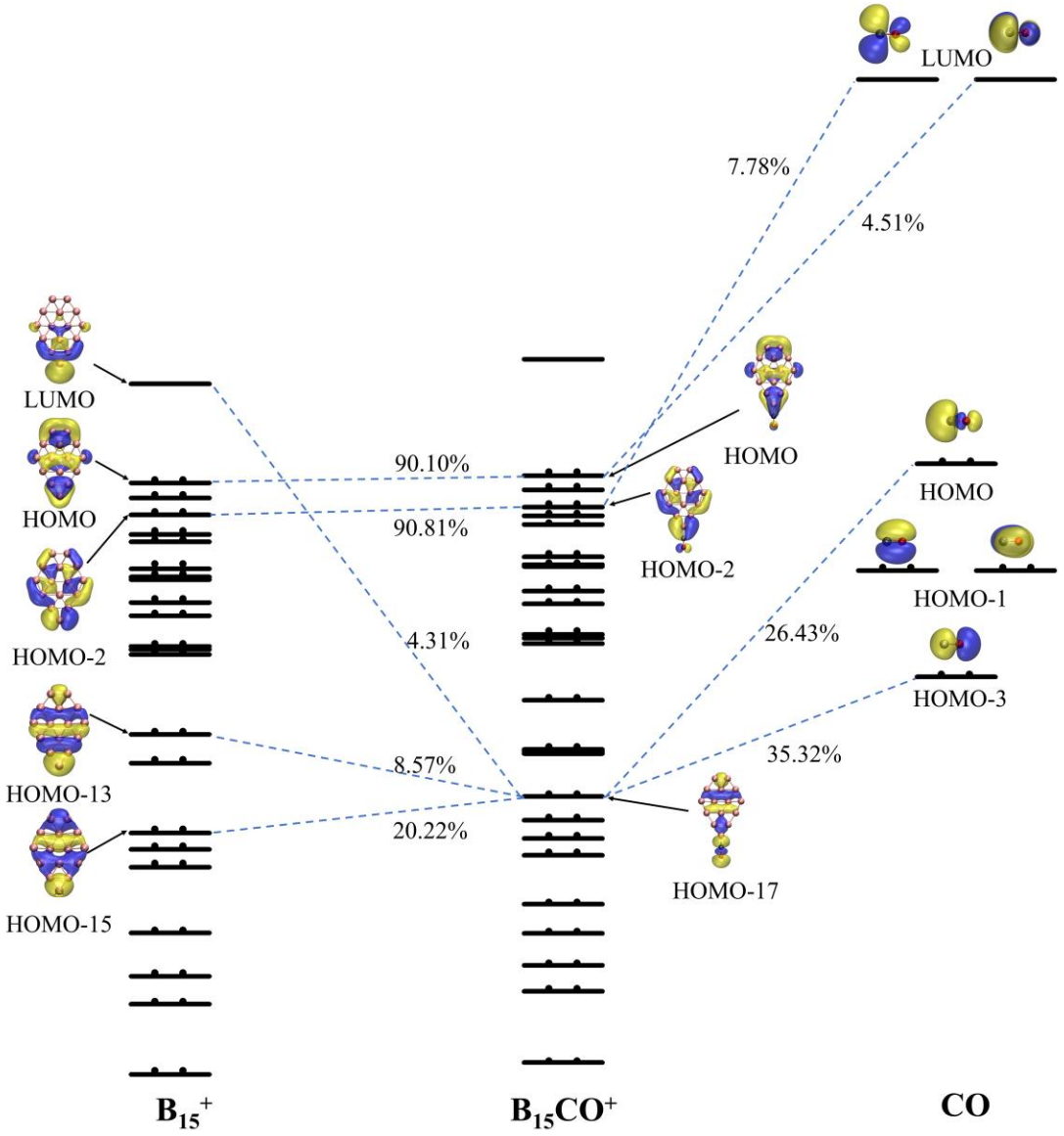

Fig. S28. Bonding scheme of $B_{15}(CO)^+$ (**15-1A**) based on EDA-NOCV analyses, with C_{2v} B_{15}^+ and CO designated as interacting fragments. Only the most important occupied valence orbitals HOMO-17 representing the effective σ-donation coordination bond and HOMO and HOMO-2 responsible for weak π-back-donations between B_{15}^+ and its ligand CO are shown, with the percentage contributions from the corresponding molecular orbitals of the fragments B_{15}^+ and CO indicated.

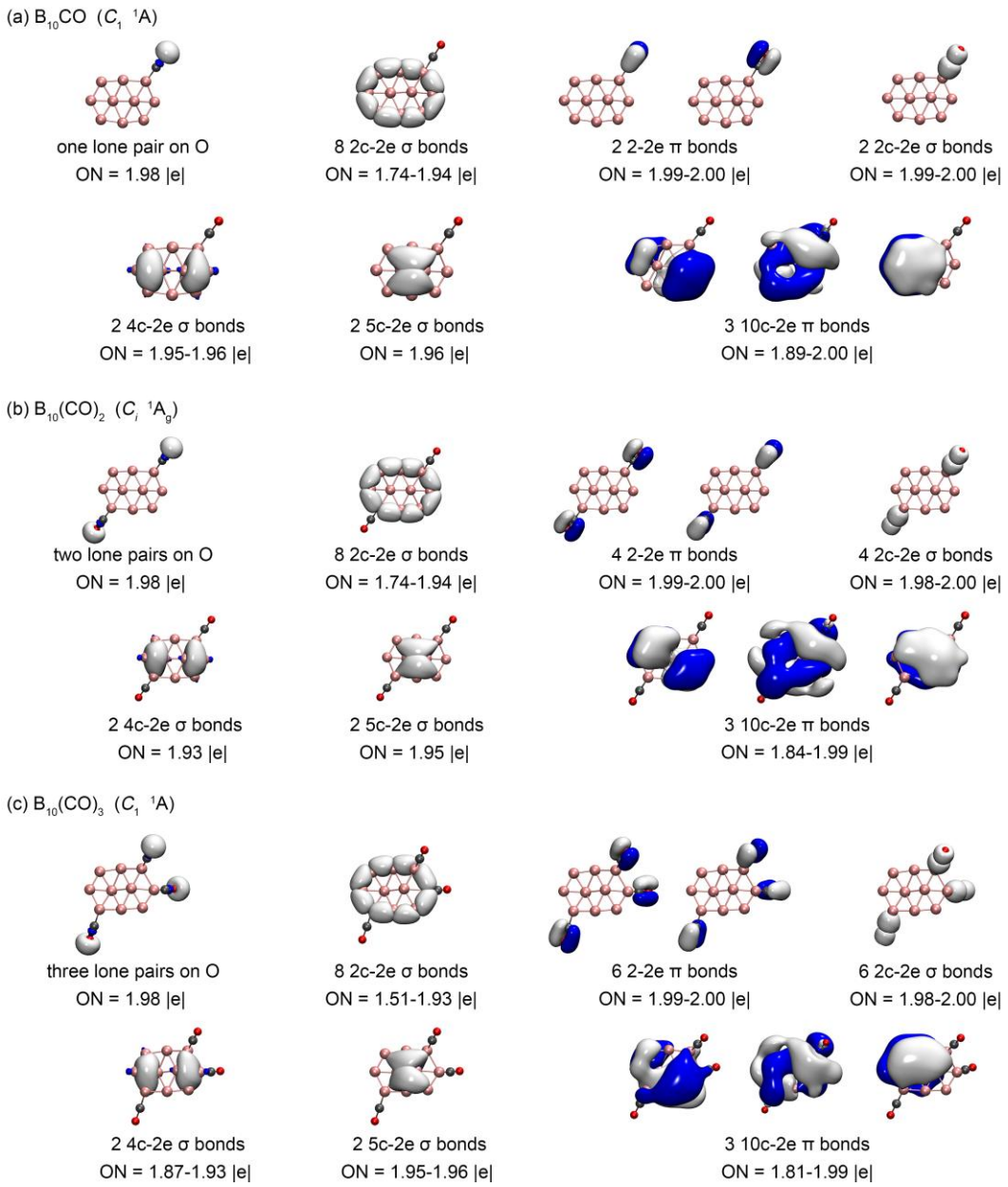

Fig. S29. AdNDP bonding patterns of (a) C_1 $B_{10}(CO)$, (b) C_i $B_{10}(CO)_2$, and (c) C_1 $B_{10}(CO)_3$, with the occupation numbers (ONs) indicated.

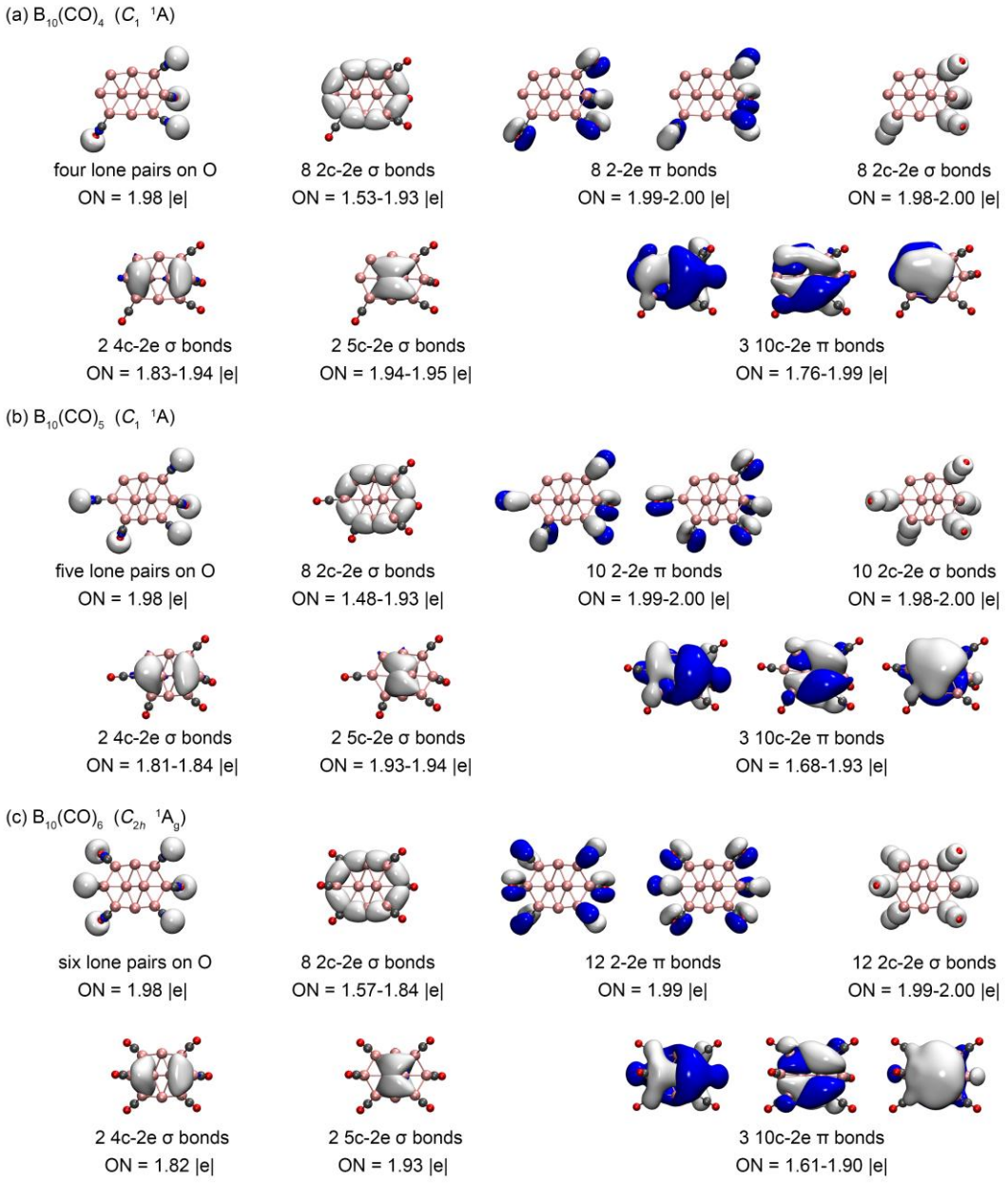

Fig. S30. AdNDP bonding patterns of (a) C_1 $B_{10}(CO)_4$, (b) C_1 $B_{10}(CO)_5$, and (c) C_{2h} $B_{10}(CO)_6$, with the occupation numbers (ONs) indicated.

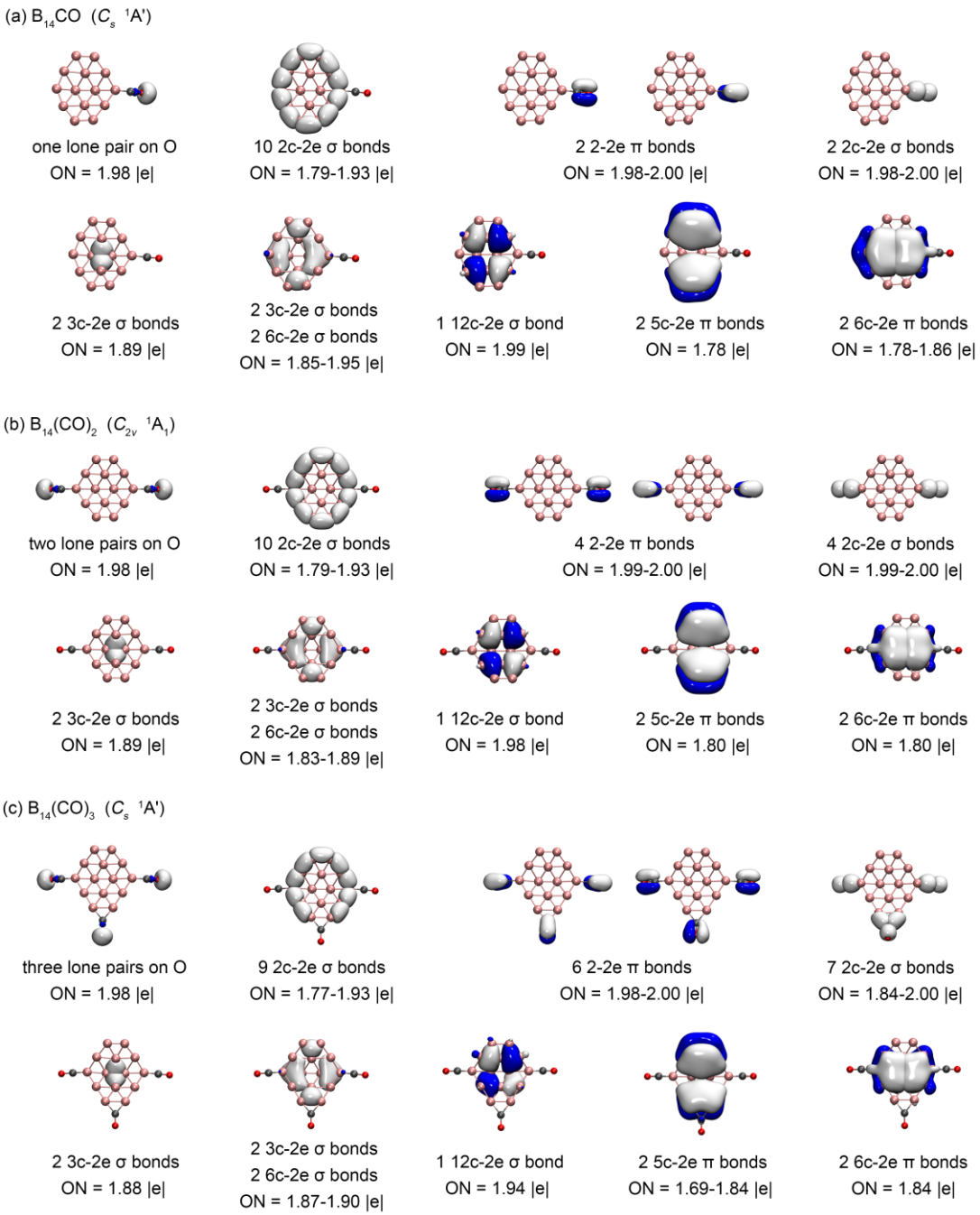

Fig. S31. AdNDP bonding patterns of (a) C_s $B_{14}(CO)$, (b) C_{2v} $B_{14}(CO)_2$, and (c) C_s $B_{14}(CO)_3$, with the occupation numbers (ONs) indicated.

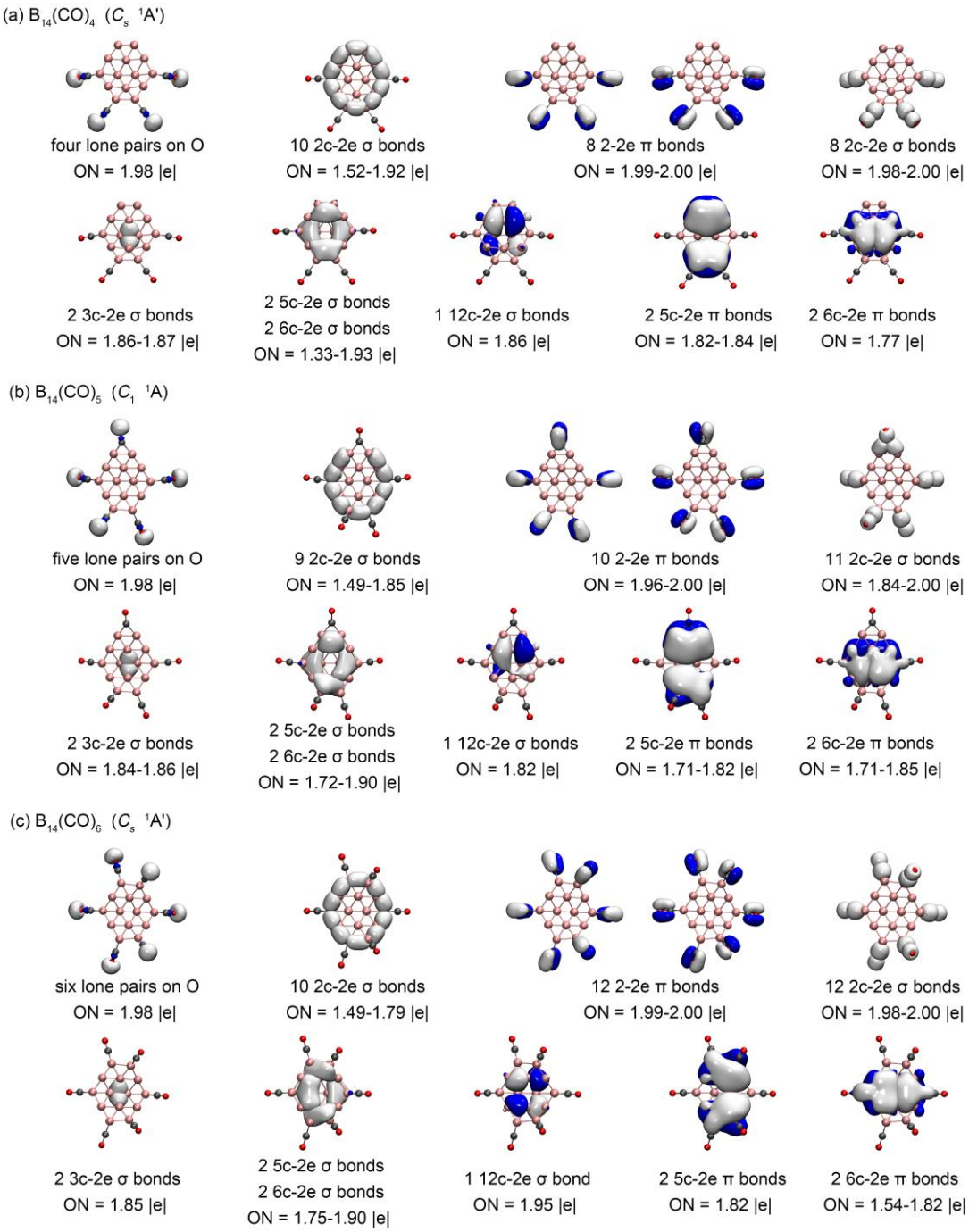

Fig. S32. AdNDP bonding patterns of (a) C_s $B_{14}(CO)_4$, (b) C_1 $B_{14}(CO)_5$, and (c) C_s $B_{10}(CO)_6$, with the occupation numbers (ONs) indicated.

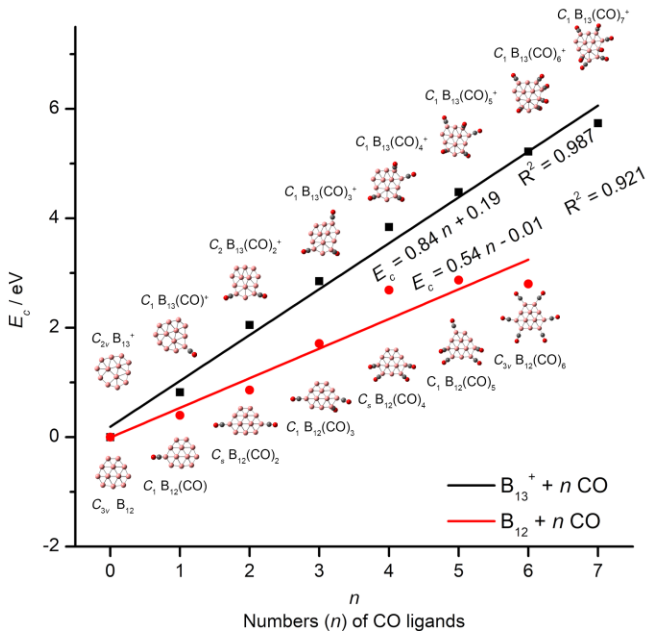

Fig. S33. Calculated chemisorption energies of $E_c = (E_{B13+} + nE_{CO}) - E_{B13(CO)n+}$ (black) and $E_c = (E_{B12} + nE_{CO}) - E_{B12(CO)n}$ (red) with respect to the number of CO ligands (n) in the systems at CCSD(T) level. The slopes of the fitted linear relationships represent the approximate average cohesive energy per CO ligand of the corresponding adsorption processes.

Table S1. EDA-NOCV results for $B_{11}(CO)^+$ (**11-1A**) at the PBE0/TZ2P-ZORA level using PBE0/6-311+G(d,p) optimized geometries, with CO and B_{11}^+ designated as the interacting fragments. Energy values are given in kcal/mol.

Energy term	Assignment	Interacting fragment $B_{11}^+ + CO$
ΔE_{int}		-75.4
ΔE_{Pauli}		157.9
ΔE_{elstat}[a]		-82.1 (35.2%)
ΔE_{orb}[a]		-151.2 (64.8%)
$\Delta E_{orb}(1)$ [b]	$[B_{11}^+(p)] \leftarrow$ CO σ donation	-102.3 (67.7%)
ΔE_{orb} (2) [b]	$[B_{11}^+(p)] \rightarrow$ CO π backdonation	-20.2 (13.3%)
ΔE_{orb} (3) [b]	$[B_{11}^+(p)] \rightarrow$ CO π backdonation	-15.2 (10.1%)
ΔE_{orb} (4) [b]		-11.5 (7.6%)
ΔE_{orb} (rest) [b]		-2.1 (1.4%)

[a] The values in parentheses give the percentage contribution to the total attractive interactions $\Delta E_{elstat} + \Delta E_{orb}$. [b] The values in parentheses give the percentage contribution to the total orbital interactions ΔE_{orb}.

Table S2. EDA-NOCV results for $B_{15}(CO)^+$ complexes at the PBE0/TZ2P-ZORA level using PBE0/6-311+G(d,p) optimized geometries, with CO and B_{15}^+ designated as the interacting fragments. Energy values are given in kcal/mol.

Energy term	Assignment	Interacting fragment $B_{15}^+ + CO$
ΔE_{int}		-82.9
ΔE_{Pauli}		176.2
ΔE_{elstat}[a]		-92.6 (35.7%)
ΔE_{orb}[a]		-166.5 (64.3%)
$\Delta E_{orb}(1)$ [b]	$[B_{15}^+(p)] \leftarrow$ CO σ donation	-106.8 (64.2%)
$\Delta E_{orb}(2)$ [b]	$[B_{15}^+(p)] \rightarrow$ CO π backdonation	-22.1 (13.3%)
$\Delta E_{orb}(3)$ [b]	$[B_{15}^+(p)] \rightarrow$ CO π backdonation	-20.6 (12.4%)
$\Delta E_{orb}(4)$ [b]		-14.7 (8.9%)
ΔE_{orb}(rest) [b]		-2.2 (1.3%)

[a] The values in parentheses give the percentage contribution to the total attractive interactions $\Delta E_{elstat} + \Delta E_{orb}$. [b] The values in parentheses give the percentage contribution to the total orbital interactions ΔE_{orb}.